

THESIS FOR THE DEGREE OF DOCTOR OF PHILOSOPHY IN THERMO AND
FLUID DYNAMICS

**Aerodynamics of an Aeroengine Intermediate
Compressor Duct: Effects from an Integrated Bleed
System**

ELÍAS MIKAEL VAGN SIGGEIRSSON

Department of Mechanics and Maritime Sciences
Division of Fluid Dynamics
CHALMERS UNIVERSITY OF TECHNOLOGY
Göteborg, Sweden 2020

**Aerodynamics of an Aeroengine Intermediate Compressor Duct: Effects from
an Integrated Bleed System**

ELÍAS MIKAEL VAGN SIGGEIRSSON

ISBN 978-91-7905-321-5

© ELÍAS MIKAEL VAGN SIGGEIRSSON, 2020

Doktorsavhandlingar vid Chalmers tekniska högskola

Ny serie nr. 4788

ISSN 0346-718X

Department of Mechanics and Maritime Sciences

Division of Fluid Dynamics

Chalmers University of Technology

SE-412 96 Göteborg

Sweden

Telephone: +46 (0)31-772 1000

Cover:

Streamlines near the hub in the intermediate compressor duct. Colored with entropy.

This document was typeset using L^AT_EX

Printed at Chalmers Reproservice

Göteborg, Sweden 2020

Aerodynamics of an Aeroengine Intermediate Compressor Duct: Effects from an Integrated Bleed System

ELÍAS MIKAEL VAGN SIGGEIRSSON

Department of Mechanics and Maritime Sciences

Division of Fluid Dynamics

Chalmers University of Technology

ABSTRACT

With the successful development of high-bypass-ratio turbofan engines, major aerodynamic components have been optimized and continuous efficiency improvements are getting harder to maintain. Therefore, to meet the requirements of lower emission of greenhouse gases, auxiliary modules such as intermediate ducts are receiving increasing interest. The Intermediate Compressor Duct (ICD) is an S-shaped duct connecting the engine's low- and high-pressure compressor systems. Improving the ICD design has the potential to favorably affect the engine's emission levels by reducing the engine's length and, therefore, its weight.

In this thesis, a state-of-the-art ICD is simulated using Computation Fluid Dynamics (CFD). The geometry of the ICD represents a test section from an experimental rig. The upstream flow conditions are essential to achieve realistic behavior in the ICD. Therefore, integrated design is considered, including a representative of the last stage from the upstream low-pressure compressor and an upstream rotor off-take bleed system. The bleed system is an auxiliary module and ensures a stable operation during off-design conditions. Through the bleed system, pressurized air is extracted from the main flow-path and used for different applications. The effect an upstream bleed system has on the ICD is analyzed, where the stability and the flow physics are compared for different bleed ratios. To take advantage of the integrated design and increasing computational resources, higher fidelity CFD simulations, using hybrid RANS/LES turbulence models, are compared to more common industrially applied CFD models and validated using experimental data.

The results show that the stability of the ICD is compromised with high bleed ratios. The flow at the low-pressure compressor's outlet guide vanes (OGVs) is separated and the separation is more severe at the inner casing. The increased separation is caused by a thicker inner casing boundary layer and the conservation of tangential momentum when extracting axial velocity through the bleed system. As a result, the ICD experiences separated flow at the critical point of diffusion. The separation at the critical point of diffusion increases in magnitude with increased bleed rates.

Comparing the hybrid models to the steady-state RANS models, the hybrid models are capable of predicting the circumferentially averaged total pressure profiles downstream of the ICD. However, the RANS simulations result in over-predicted losses due to over-predicted separation on the OGV blades. The experimental data had a relatively low resolution, and therefore, the hybrid methods need further validations. Furthermore, the hybrid methods are significantly more expensive but represent the transient flow field, whereas the RANS simulations only provide the time-averaged results.

Keywords: CFD, Turbomachinery, Intermediate Compressor Duct, S-shaped duct, Bleed system, rotor off-take, Hybrid RANS/LES, DDES, SBES, Dual-time-stepping

ACKNOWLEDGEMENTS

I would like to thank my supervisors who gave me the opportunity to become a Ph.D. student: Niklas Andersson at Chalmers, and Fredrik Wallin and Markus Burak at GKN Aerospace, for their never-ending support and guidance. I would also like to thank Marcus Lejon for always showing interest in my work and being available.

I would like to give Adam Jareteg special thanks for always being up for discussions and teaching me what I know in the Swedish language (still not sure if you should take that as a complement or not). The G3D::Flow crew, Daniel and Gonzalo, for all the tears and glories shared over the years. My friends from Iceland, Ragnar, for teaching me everything I know and Steinn, those hunting trips really made a difference. I would also like to thank all my colleagues and friends over the years, wherever you are.

My family, you have given me the possibility to follow my dreams by always supporting me, thank you. To my daughter Þórey Elísabet, you really bring joy to my live. Last, but definitely not least, thank you Guðrún, where would I be without you!

This research work was funded by the Swedish National Aviation Engineering Research Programme, NFFP with financial support from VINNOVA and the Swedish Defense Material Administration (FMV). The author would like to acknowledge GKN Aerospace for the permission to publish their work. All CFD simulations were performed using SNIC (Swedish National Infrastructure for Computing) resources at the National Supercomputer Center in Sweden, NSC.

Elías Mikael Vagn Siggeirsson
Göteborg, May 2020

To Guðrún

NOMENCLATURE

Hub	–	Inner casing
Casing	–	Outer casing
Span	–	$\frac{r-r_{\text{hub}}}{r_{\text{casing}}-r_{\text{hub}}} \cdot 100\%$
 Latin symbols		
u_i	–	Cartesian components of velocity vector
u, v, U, V	–	Cartesian velocity components
L	–	Characteristic length
Re	–	Reynolds number
x_i	–	Cartesian coordinate vector component
c	–	Speed of sound
C_p	–	Specific heat at constant pressure,
	–	Static pressure coefficient
C_P	–	Total pressure coefficient
C_v	–	Specific heat at constant volume
C_S	–	Smagorinsky model coefficient
e, E	–	Energy
h	–	Enthalpy
k	–	Kinetic energy, thermal conductivity
p	–	Static pressure
P	–	Total pressure, pre-conditioning matrix
q	–	Heat flux
M	–	Mach number
Pr	–	Prandtl number
S_{ij}	–	Strain rate tensor
T	–	Temperature
t	–	Time
f_d	–	DDES shielding function
C_{DDES}	–	DDES coefficient
\tilde{d}	–	DDES length-scale
r_d	–	DDES function
f_s	–	SBES shielding function
R	–	Spatial residuals, gas constant
Q	–	State vector in equations on conservative form
I, J, K	–	Grid coordinates
d	–	Wall-distance
A	–	Area
V	–	Volume
t	–	Blade thickness
c	–	Blade chord
$f_{v1}, f_2, f_w, f_{t2}, g, r$	–	SA-turbulence model functions
$c_{b1}, c_{b2}, c_{w1}, c_{w2}, c_{w3}, c_{v1}, c_{t3}, c_{t4}$	–	SA-turbulence model coefficients

Greek symbols

ρ	– Density
Δ	– Filter width
μ	– Dynamic viscosity
ν	– Kinematic viscosity
σ_{ij}	– Viscous stress tensor
σ	– SA-turbulence model coefficient
τ_{ij}	– Turbulent stress tensor
δ_{ij}	– Kronecker delta tensor
τ	– Pseudo time
$\tilde{\nu}$	– SA-viscosity
ν_t	– Turbulent viscosity
α	– Runge-Kutta coefficient, preconditioning coefficient
Δt	– Time-step
$\Delta \tau$	– Pseudo time-step
Λ	– Matrix of characteristic speeds
κ	– Wavelength, SA-turbulence model coefficient

Superscripts

–	– Ensemble averaged quantity, spatially filtered quantity
'	– Resolved fluctuations
''	– Unresolved fluctuations
^	– Spatially Favre-filtered quantity
~	– Mass-flow averaged quantity
(0)	– Initial solution
(k)	– RK stage
(l)	– Inner iteration
n	– Time-step

Subscripts

c	– Matrix on conservative form
in	– Inlet
ex	– Outlet
sgs	– Sub-Grid-Scales

Abbreviations

CFD	– Computational Fluid Dynamics
LPC	– Low Pressure Compressor
HPC	– High Pressure Compressor
CC	– Combustion Chamber
HPT	– High Pressure Turbine
LPT	– Low Pressure Turbine
ICD	– Intermediate Compressor Duct
OGVs	– Outlet Guide Vanes
IGVs	– Inlet Guide Vanes

LES	– Large Eddy Simulation
RANS	– Reynolds-Averaged Navier-Stokes
CPUs	– Central Processing Units
DNS	– Direct Numerical Simulations
URANS	– Unsteady RANS
SGS	– Sub-Grid-Scales
SA	– Spalart-Allmaras turbulence model
SST	– $k - \omega$ SST turbulence model
DES	– Detached Eddy Simulation model
DDES	– Delayed Detached Eddy Simulation model
SBES	– Stress-Blended Eddy Simulation model
RK	– Runge-Kutta
DT	– Dual-Time-stepping
IRSM	– Implicit Residual SMOOTHing
AR	– Aspect Ratio
PSW	– Pre-Swirl
LE	– Leading edge
TE	– Trailing edge

THESIS

This thesis consists of an extended summary and the following appended papers:

- Paper A** E. M. V. Siggeirsson, N. Andersson, and F. Wallin. “Sensitivity study of the SA-DDES shielding function”. *AIAA Scitech 2018 Forum*. Kissimmee, Florida, 2018
- Paper B** E. M. V. Siggeirsson, N. Andersson, and F. Wallin. “Numerical and experimental study on bleed impact on intermediate compressor duct performance”. *ASME 2018, Turbo Expo*. Oslo, Norway, 2018
- Paper C** E. M. V. Siggeirsson and N. Andersson. “The NASA 2D wall-mounted hump simulated using DDES-SA with the G3D::Flow solver”. *AIAA Scitech 2019 Forum*. San Diego, California, 2019
- Paper D** E. M. V. Siggeirsson, N. Andersson, and M. O. Burak. “Integrated Compressor Duct with Bleed: Experimental Validation of a Hybrid RANS/LES Approach”. *24th ISABE Conference*. Canberra, Australia, 2019
- Paper E** E. M. V. Siggeirsson, N. Andersson, and M. O. Burak. “Off design simulations of an S-shaped intermediate compressor duct: Experimental validation of DDES and RANS using G3D::Flow”. *AIAA Scitech 2020 Forum*. 2020
- Paper F** E. M. V. Siggeirsson, N. Andersson, and M. O. Burak. Numerical and Experimental Aerodynamic Investigation of an S-shaped Intermediate Compressor Duct with Bleed. *Accepted for publication in Journal of Turbomachinery* (2020)
- Paper G** E. M. V. Siggeirsson, N. Andersson, and M. Lejon. Integrated compressor duct aerodynamics with an integrated rotor off-take bleed. *Submitted to an AIAA Journal* ()

CONTENTS

Abstract	2
Abstract	i
Acknowledgements	iii
Nomenclature	vii
Thesis	xi
Contents	xiii
I Extended Summary	1
1 Introduction	2
1.1 The aircraft engine	2
1.2 Intermediate compressor duct	4
1.3 Bleed air	5
1.4 Aim	7
2 Computational Fluid Dynamics	9
2.1 Governing equations	9
2.2 Turbulence modeling	10
2.3 URANS	13
2.4 LES	16
2.5 Hybrid RANS/LES	16
2.5.1 DDES	17
2.5.2 ANSYS SBES	18
2.6 Spatial discretisation	19
3 Acceleration Techniques	20
3.1 Verification	24
4 Retrospective view	27
4.1 Pre-swirler	27
4.1.1 Horseshoe vortex	27
4.1.2 PSW representing a rotor	28
4.2 OGV	29
4.2.1 OGV separation	30
4.3 ICD with an integrated strut	32
4.4 Data normalization	38

4.5	Conclusion	39
5	Summary of papers	41
5.1	Paper A	41
5.2	Paper B	42
5.3	Paper C	44
5.4	Paper D	45
5.5	Paper E	46
5.6	Paper F	50
5.7	Paper G	50
6	Concluding Remarks	52
6.1	Future Work	53
	References	54
II	Appended Papers	61

Part I
Extended Summary

Chapter 1

Introduction

Air traffic has increased rapidly over the last decades, leading to a global increase in emissions of CO₂ and other greenhouse gases. This increase can be locally retarded by replacing old aircraft with newer ones [5], but this effect is unlikely to be sustained since all forecasts anticipate exponential growth in air traffic over the coming years [4, 32]. To make flight more sustainable over a longer period of time, continuous performance improvements are needed, where improving the efficiency of aircraft engines will be an important factor.

The efficiency of aircraft engines has improved significantly in recent decades, especially due to the widespread use of Computational Fluid Dynamics (CFD) simulations. The use of CFD has enabled the development of high bypass-ratio turbofan engines with large fans and high pressure-ratio engine cores, combining relatively high efficiencies, high sub-sonic aircraft velocities, and low noise levels. Unfortunately, further efficiency improvements are getting harder to achieve using the current design process.

In the design process, engine components are usually divided into several modules, each of which is optimized separately where the effects from surrounding modules are modeled or simplified to some extent. Ghisu et al. [26] showed that optimizing components in isolation from each other can yield a sub-optimal overall engine design, which may necessitate expensive redesign work late in the design process. The risk of a sub-optimal design can be substantially reduced by adopting more integrated design processes in which multiple components are optimized and/or studied together. Such integrated processes take advantage of the reduced need for simplified or modeled interactions between components, yielding better results at an earlier stage [25, 26, 76].

1.1 The aircraft engine

Figure 1.1 presents an example of a modern high bypass-ratio turbofan engine, whereas Figure 1.2 shows a simplified schematic, where only major components and flow-paths are visible. Modern high bypass-ratio turbofan engines have six major aerodynamic components. The fan, which is located at the engine inlet, is the first stage of compression. The fan accelerates the air where a fraction of the air enters the engine core, whereas most of it is bypassed. The flow through the engine's core provides the necessary power to run the engine. The bypassed air is, however, responsible for the majority of the engine's thrust. Newer high bypass-ratio turbofan engines typically have a bypass-ratio of 8-12. This means that for every 8-12 kg of bypassed air, 1 kg enters the engine core.

Located in the front part of the core, the low- and high-pressure compressors (LPC and HPC, respectively) perform the second and third stages of compression, respectively. The combustion chamber (CC) is where the fuel is injected into the compressed air and ignited to increase the energy of the fluid. The high-pressure turbine (HPT) is where energy is extracted from the core flow to drive the HPC. The final major aerodynamic component is the low-pressure turbine (LPT). In a three-spool configuration, the LPT

is divided into two turbines, each of which drives a different shaft to establish different rotational speeds for the fan and the LPC. In a two-spool engine configuration, the LPT drives both the LPC and the fan, where the different rotational speeds are established using a geared shaft.

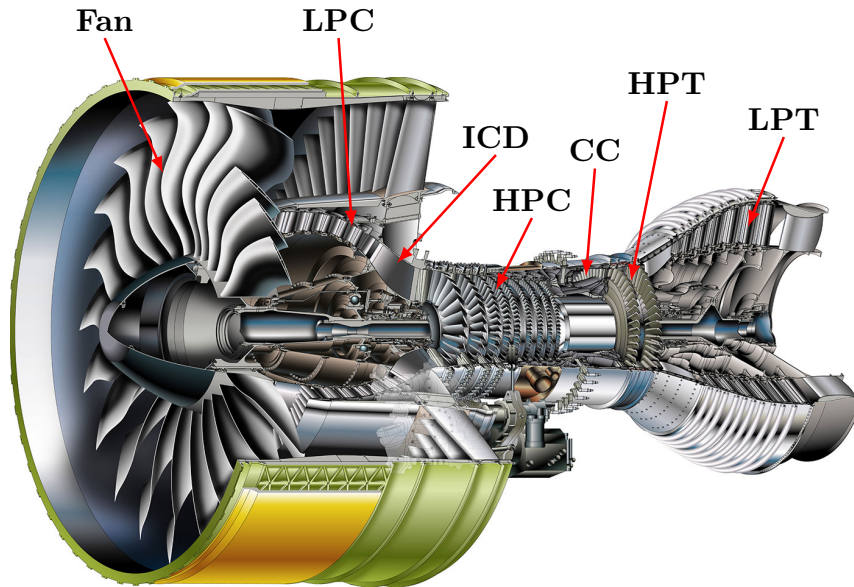


Figure 1.1: *The two spool GP7000 turbofan engine [31].*

The major aerodynamic components, such as the compressor and turbine modules, have been studied and optimized to a great extent. There has, however, not been as much focus on designing the auxiliary systems, where only stationary components are included. The importance of addressing those systems to improve the overall engine efficiency is increasing. As an example, improvements in intermediate ducts, located between the major components, can result in shorter and, therefore, lighter engines, increasing the total efficiency of the engine.

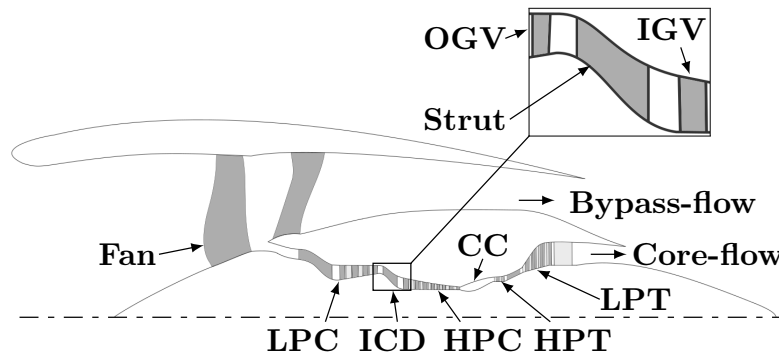


Figure 1.2: *A schematic of a turbofan engine. Blades are colored with gray.*

1.2 Intermediate compressor duct

The intermediate compressor duct (ICD) is an S-shaped duct located between the LPC and the HPC. The ICD is important for the engine operation but the analysis and improvements of the ICD's performance have attracted less interest compared to the major components. The purpose of the ICD is to guide the flow from the larger exit radius of the LPC towards the smaller inlet radius of the HPC. The LPC tends to have a large radius to achieve more efficient compression, whereas the HPC has a lower radius to limit tip leakage losses and reduce disk weight. The ICD forces the flow through the radial offset with minimal axial length to limit the engine's size and weight. Furthermore, the ICD should be designed for high efficiency and to deliver as undisturbed flow as possible to the HPC's Inlet Guide Vanes (IGVs). These competing requirements necessitate an aggressive duct design. If the radial forcing is too aggressive, strong adverse pressure gradients may develop, potentially causing the flow to separate. In the upper right corner of Figure 1.2, a detailed view of the ICD is presented. The Outlet Guide Vanes (OGVs) of the upstream LPC and the IGVs of the downstream HPC can be seen, along with the radial offset between the two compressors. Furthermore, a stationary blade row (strut) is integrated into the ICD to add mechanical strength and allow for service pipes and electrical wiring to the engine's core.

Several authors have examined the flow-physics found in an S-shaped duct. Bradshaw [12] studied the curvature effects of concave and convex surfaces. The author showed that turbulence levels are reduced over a convex surface and induced over a concave surface. Britchford et al. [14] analyzed the flow field of an S-shaped duct and concluded that the flow inside such ducts is complex and influenced by their strong curvature and the stream-wise pressure gradient, increasing the high risk of separation at the inner wall. Bailey et al. [10] showed that the pressure losses in an S-shaped duct with a well-behaved flow and no separation were comparable to those for a parallel-sided duct despite the strong curvature and pressure gradient effects. The authors also showed that the presence of a strut, integrated into the S-shaped duct, imposed blockages that increased pressure losses, resulting in the formation of thicker boundary layers at the inner and outer casings. Britchford et al. [13] showed that an upstream rotor could efficiently re-energize the boundary layer at the inner wall and thereby reduce the adverse pressure gradient, resulting in a lower risk of separation. The boundary layer shape-factor decreased from 1.65, for a "clean" inlet, to 1.47 with an upstream compressor. Sonoda et al. [60] measured and simulated the performance of an S-shaped duct for two different inlet boundary layer thicknesses. The overall losses increased with an increased boundary layer thickness (33% and 23% increase in losses for the measurements and simulations, respectively). The large difference for the increased losses was mainly caused by over-prediction of losses near the casing in the simulations. Ortiz et al. [47] performed measurements and simulations on three different ducts, where the longest duct represented a state-of-the-art duct design. The other ducts had 74% and 64% of the original duct's length. The radial turning angle of each duct was optimized to minimize losses. The 74% duct showed signs of a small increase in losses, compared to the datum design, whereas the 64% duct, resulted in a significant increase. However, the authors concluded that the current design methods are conservative, limiting the design space. Karakasis et al. [36] compared the performance of

axisymmetric and non-axisymmetric ducts with experiments and CFD simulations. The simulations agreed well with the experimental data for the flow near the hub but did not accurately capture the behavior near the casing. Including an upstream compressor stage increases the total pressure loss in the duct by 54% for the axisymmetric duct and 28% for the non-axisymmetric duct. The paper gives a good description of the mechanics in an ICD with a strut and an upstream compressor. Naylor et al. [45] designed two "clean" S-shaped ducts with different lengths: 100% and 74%. Both ducts were highly loaded and near the limit of an attached flow. By integrating struts into the S-shaped ducts, the flow diffused towards the trailing edge, resulting in separation at the strut-hub intersection. The strut-hub separation increased losses by 50% and 88% for the 100% and 74% ducts, respectively. Furthermore, the authors showed that by using non-axisymmetric end-wall profiling, the strut-hub separation could be eliminated. Walker et al. [76] presented a design with the LPC's OGVs integrated into the ICD. A comparison was made between the integrated design and a conventional datum design, where the OGVs were located upstream of the ICD. The integrated design resulted in a 21% shorter system, with a 4% increase in losses, emphasizing the necessity for integrated designs.

While the ICD has not been optimized to the same extent as the major components, there have been some successful attempts, in addition to the previously mentioned papers, to optimize or analyze the design. For example, Stürzebecher et al. [66] performed an optimization with non-axisymmetric end-walls and a lifting strut. The length of the duct was reduced by 19% with 2% reduction in losses. Additionally, the authors showed that the exit swirl from the OGV and the ICD was dependent on if the boundary layers were resolved or modeled, even though the axial velocity, the static pressure and the total pressure were in a good agreement. Several other papers exist on the optimization of S-shaped ducts [44, 39, 20]. Those papers showed that there is a potential for shorter and lighter engines with more aggressive flow guidance.

With the studies mentioned above, there are still limited practical design rules for ICDs. Therefore, the design is usually guided by a combination of CFD and isolated optimization studies [66]. The interaction between the duct and the surrounding systems has not been addressed extensively, even though it can strongly affect the performance. If this interaction is neglected, the isolation of the ICD during the design process can limit the design space because the duct's internal flow field depends strongly on the surrounding systems. Consequently, a more integrated design strategy in which the surrounding systems are introduced earlier in the design process should be considered. One of the coupled systems is the integrated bleed system, where air is extracted from the main flow-path upstream of the ICD.

1.3 Bleed air

Flow extracted from the main flow-path in the compression system is usually referred to as bleed air. The flow is extracted through a bleed system which is connected to the main flow-path with a bleed pipe. The following list shows the necessity of the bleed system for the operation of the engine and the aircraft.

- Cooling air for high-temperature structures, such as combustor and turbine blades

and discs:

- There is a great benefit from achieving higher temperatures in the turbine of an aircraft engine. With higher temperatures, an increase in specific thrust (thrust per unit mass-flow of air) is possible. Even though advanced materials are used for the high-temperature structures, the temperatures are limited by the material's melting point. Therefore, to increase the turbine temperature, cooling air is used to cool the hot components. With increasing turbine temperatures, the required amount of cooling air is increasing, making the bleed system a more interesting research topic.
- Pressurizing cavities and bearings:
 - It is very expensive to manufacture water-tight components. Therefore, pressurized air is used to ensure that fluid with temperatures above the material's melting point does not reach vulnerable components.
- Handling bleed:
 - Handling bleed is used to limit the risk of surge at engine start and compressor off-design conditions. At off-design conditions, for example, decent, the LPC would operate closer to surge, due to lower rotational speed. However, by increasing the mass-flow through the LPC, the surge margin can be increased. To obtain the correct mass-flow through the HPC, a fraction of the LPC air is extracted through a bleed pipe in-between the LPC and the HPC. The HPC is not as sensitive to the decreased rotational speed as the LPC.
- Air used for heating structures vulnerable to icing, such as wings and blades:
 - Ice formation imposes significant risk for the aircraft operation, where ice can severely impact the performance of the aircraft and the engine (the geometry of aerodynamically important structures can be reshaped due to ice formations). The air extracted from the compression system has a relatively high temperature and is therefore distributed to vulnerable structures.
- Particle extraction, such as large water droplets and hails:
 - When the compressor is exposed to large quantities of water, the operating line is shifted towards the surge line, decreasing the surge margin. The surge margin is further decreased if the water droplets are replaced with ice. Furthermore, if a large amount of water/ice is ingested, it may lead to a total flame-out. It is of great interest to extract the particles as far upstream as possible to limit the effect on the engine. The bleed pipe is integrated into the concave turning in the casing downstream of the LPC to capture larger particles [3].
- Cabin air:
 - Provides the airplane cabin with pressurized air.

The performance of a compressor bleed system is getting increasing attention. Leishman et al. [38] studied three bleed configurations using linear cascade experiments. For the three configurations, the bleed pipe was: (1) integrated into the compressor casing in-between the rotor blades; (2) a part of the trailing edge of the rotor blades; (3) and integrated downstream of the rotor blades (rotor off-take). The first two configurations showed evidence of increased system losses, whereas the rotor off-take showed a decrease in overall blade passage losses. The decreased losses were caused by the end-wall boundary layer being extracted from the blade passage.

Chen et al. [16] studied four different bleed locations, integrated into the casing of a rotor, by performing 3D CFD simulations. Furthermore, a single outlet duct was used for the 360°, causing non-uniformity in the flow. The non-uniformity was insignificant for a low bleed ratio (1% bleed) but for higher bleed ratios (3% and 5% bleed), the non-uniformity became more severe. However, no estimation was given on the losses introduced by the bleed system but extracting the low momentum boundary layer at the casing decreased the losses in the compressor.

Grimshaw et al. [27] studied non-uniformities in a compressor stage where the bleed pipe was located upstream of the rotor. Both CFD and experiments were conducted, where unsteady simulations gave accurate predictions of the measurements. Grimshaw et al. [28] compared different bleed systems: a continuous bleed outlet, a single bleed outlet duct and two bleed outlet ducts. The sparse outlet ducts created static pressure distortions in the main flow-path resulting in circumferential variations in the downstream flow-coefficient. The distorted flow emphasizes the importance of taking the whole bleed system into account. Additionally, part of the boundary layer at the casing was extracted through the bleed pipe, causing a radial redistribution of the axial velocity. Grimshaw et al. [29] presented a generic method to quantify the characteristic losses in a bleed system. The authors applied the loss calculation on a research compressor and an industrial gas turbine compressor. For both compressors, most losses were observed for the pipe integrated into the compressor casing. Walker et al. [74] introduced a bleed pipe integrated into the transition between the convex and concave turning at the inner casing of an ICD. The main purpose of the bleed flow was to remove the weak boundary layer, lowering the risk of separation and allowing for shorter ICD design. The boundary layer was accelerated into the bleed pipe, where the shear-layer between the boundary layer and the free-stream re-energized the flow, extending the ICD's stability margin. What the previously mentioned papers [16, 28, 28, 29, 74] have in common is the relatively low bleed fraction, compared to the maximum of 40% bleed ratio analyzed in this thesis.

The flow physics, when integrating the bleed pipe into the casing of a compressor, are well known. However, the interaction between the ICD, the upstream LPC and the integrated bleed system, when the bleed system is integrated into the ICD (rotor off-take [1, 2]), has not been addressed properly. A rotor off-take bleed is the only bleed configuration considered in this thesis.

1.4 Aim

The aim of this thesis can be divided into two categories

1. Achieve a deeper understanding of the flow physics in an ICD with an integrated bleed system and the last stage of the upstream LPC.

As discussed in the previous sections, there is a lack of understanding in the interactions between the ICD, upstream LPC and an integrated bleed system. This thesis, with appended papers, will provide a deeper understanding on:

- a) How the flow in the ICD is altered due to an upstream extraction of flow through the casing (Paper B, Paper D, Paper E, Paper F, Paper G and Chapter 4).
- b) The circumferential non-uniformity caused by the full bleed system (Paper F).
- c) Answer if the common industrial CFD methods are capable of predicting the behavior of the integrated system (Paper B, Paper D, Paper E and Paper F).
- d) Apply higher fidelity CFD methods on the integrated system. The higher fidelity models provide deeper understanding of the complicated flow features present in the ICD (Paper D, Paper E and Paper F).

2. Method development.

To improve the application of G3D::Flow, which is a CFD solver developed and maintained at the Division of Fluid Dynamics at Chalmers University of Technology. To evaluate the performance of G3D::Flow and analyze applications in uncharted areas. The evaluation highlights areas where improvements are needed, leading to the development of a more competitive solver (Paper A, Paper B, Paper C, Paper E and Chapter 3).

Chapter 2

Computational Fluid Dynamics

CFD simulations are used to get a deeper understanding of the flow behavior in the integrated system. It is relatively inexpensive to perform simulations, compared to physical experiments and therefore, CFD is a necessary tool to explore different designs. To take full advantage of the CFD simulations and the integrated design process, one should use tools such as Large Eddy Simulation (LES) models. The LES models can describe flow separation and complicated flow structures that are not fully captured by the more common Reynolds-Averaged Navier-Stokes (RANS) models. However, LES simulations are very computationally expensive. In an attempt to limit the computational cost of the LES simulations, while still capturing phenomena described poorly by RANS models, this thesis explores the application of hybrid RANS/LES models. The hybrid models combine the ability of LES to resolve the transient features of the main flow with the ability of RANS models to model attached near-wall behavior with reasonable grid densities.

Two CFD solvers are used through the extent of this thesis, G3D::Flow and ANSYS CFX. G3D::Flow is a finite volume CFD solver for compressible flows that is developed and maintained at the Division of Fluid Dynamics at Chalmers University of Technology. It is based on a family of codes developed by Eriksson [22]. For details, see the work of Eriksson [22] or Andersson et al. [6] and Chapter 3. ANSYS CFX (release 19.1) [7] is a commercial CFD solver which has proven successful in generating results for turbomachinery applications in a relatively short time. The robustness is the main reason for using a commercial solver. However, most commercial software are expensive and limited in terms of licenses, especially when considering larger simulations that require multiple central processing units (CPUs). The limited number of licenses available for each simulation (and therefore a limited number of CPUs) is a drawback when performing high fidelity simulations. Therefore, the development of solvers such as G3D::Flow is necessary.

2.1 Governing equations

The governing equations for continuity, momentum, and energy, which are solved by CFD solvers, are presented in Eq. 2.1, which are commonly referred to as the Navier-Stokes equations. In compressible, unsteady and viscid form, they are:

$$\begin{aligned} \frac{\partial \rho}{\partial t} + \frac{\partial (\rho u_j)}{\partial x_j} &= 0 \\ \frac{\partial (\rho u_i)}{\partial t} + \frac{\partial (\rho u_i u_j)}{\partial x_j} &= -\frac{\partial p}{\partial x_i} + \frac{\partial \sigma_{ij}}{\partial x_j} \\ \frac{\partial (\rho e_0)}{\partial t} + \frac{\partial (\rho e_0 u_j)}{\partial x_j} &= -\frac{\partial p u_j}{\partial x_j} + \frac{\partial}{\partial x_j} \left(C_p \frac{\mu}{Pr} \frac{\partial T}{\partial x_j} \right) + \frac{\partial}{\partial x_j} (u_i \sigma_{ij}) \end{aligned} \quad (2.1)$$

where σ_{ij} is the viscous stress tensor

$$\sigma_{ij} = \mu \left(2S_{ij} - \frac{2}{3}S_{mm}\delta_{ij} \right), \quad (2.2)$$

S_{ij} is the strain rate tensor

$$S_{ij} = \frac{1}{2} \left(\frac{\partial u_i}{\partial x_j} + \frac{\partial u_j}{\partial x_i} \right) \quad (2.3)$$

and Pr is the Prandtl number

$$Pr = \frac{\mu C_p}{k} \quad (2.4)$$

C_p is the specific heat, μ the dynamic viscosity and k the thermal conductivity. The gas is assumed to be calorically perfect because all simulations reported in this thesis were performed under atmospheric conditions. This assumption implies that the gas obeys the ideal gas law and its internal energy and enthalpy are linear functions of the temperature

$$\begin{aligned} e &= C_v T \\ h &= C_p T \\ C_v &= C_p - R \end{aligned} \quad (2.5)$$

To solve this set of equations, all scales down to the smallest scales (Kolmogorov scales) must be resolved. However, as will be discussed in the next section, this would require Direct Numerical Simulations (DNS) where the use of computationally unaffordable spatial and temporal resolutions would be required. Limitations on available computational resources means that such approaches will not be practical for the foreseeable future. Consequently, modeling techniques such as turbulence modeling, are needed to close the set of equations.

2.2 Turbulence modeling

Turbulence is a three-dimensional, chaotic and unsteady phenomenon governed by the Navier-Stokes equations, which are presented in the previous section. It controls most flows known in real-life situations, for example, the flows around cars, airplanes and trains, as well as high-speed internal flows. Its chaotic nature makes it difficult to simulate, typically necessitating at least some use of modeling techniques.

Flow situations, which are governed by inertial forces over viscous forces, are referred to as turbulent flows. The ratio of inertial forces to the viscous forces is defined as the Reynolds number

$$Re = \frac{\rho U L}{\mu} \quad (2.6)$$

Here, ρ is the fluid density, U is a characteristic velocity, L is a characteristic length scale, and μ is the fluid's dynamic viscosity. If the equation were applied to annular channel flow, U would be the mean velocity over the cross-sectional area and L would be the difference in diameter between the inner and outer walls of the annulus. The Reynolds

number is used to distinguish between laminar and turbulent flows, where turbulent flows have high Reynolds numbers.

Turbulent flows are considered to consist of combinations of swirling structures of different sizes, which are usually referred to as eddies. The larger eddies extract their energy from the mean flow. They are unstable and eventually break down into smaller eddies, with kinetic energy being transferred from the larger eddies to the smaller ones. The smaller eddies then undergo the same process, breaking up until they become so small that the fluid’s kinetic energy is dissipated into internal energy because of the fluid’s viscous stresses. This process is usually referred to as the cascade process [17]. The cascade process is depicted in the energy spectrum shown in Figure 2.1. In the figure, the energy of the eddies is plotted against their wavelength, κ . The figure can be divided into three sections: Section I of the energy spectrum corresponds to the extraction of kinetic energy from the mean flow and the breakdown of the largest eddies. Section II corresponds to the transfer of kinetic energy from larger eddies to smaller ones. Section III corresponds to the dissipation of the smallest eddies’ kinetic energy into the fluid’s internal energy. Kolmogorov’s similarity hypotheses [17] states that the kinetic energy of the intermediate eddies (*i.e.* those within section II) is governed solely by the rates of transfer from the large eddies (section I) and dissipation of the smaller ones (section III). Furthermore, at a certain size, the eddies become statistically isotropic and all information about their geometrical features is lost. The quantitative description of these processes is known as turbulence modeling.

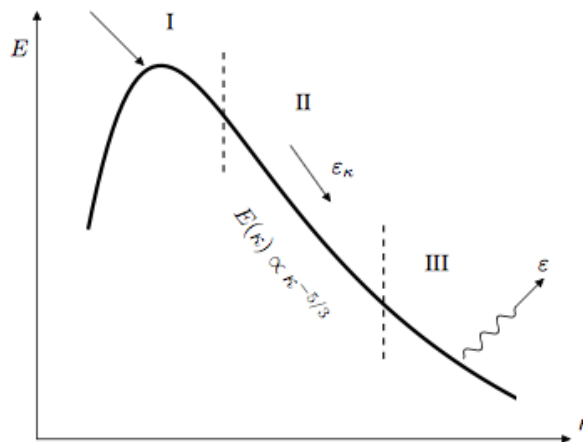


Figure 2.1: *Energy spectrum [18]*

There are several techniques to treat the cascade process. Figure 2.2 illustrates the differences between some of the most common modeling techniques in terms of their ability to resolve (as opposed to merely model) turbulent behavior in different sections of the turbulent energy spectrum. The simplest modeling techniques are the RANS family of models, which model all turbulence by time-averaging the governing equations. By time-averaging the governing equations, the time-accuracy of the flow field is replaced by faster convergence. The RANS models can provide valuable information about global quantities such as total pressure losses and mean velocities. Conversely, the Unsteady

RANS (URANS) family of models use a global time-step, allowing the very largest scales to be resolved. For both RANS and URANS, relatively large spatial and temporal resolution is sufficient.

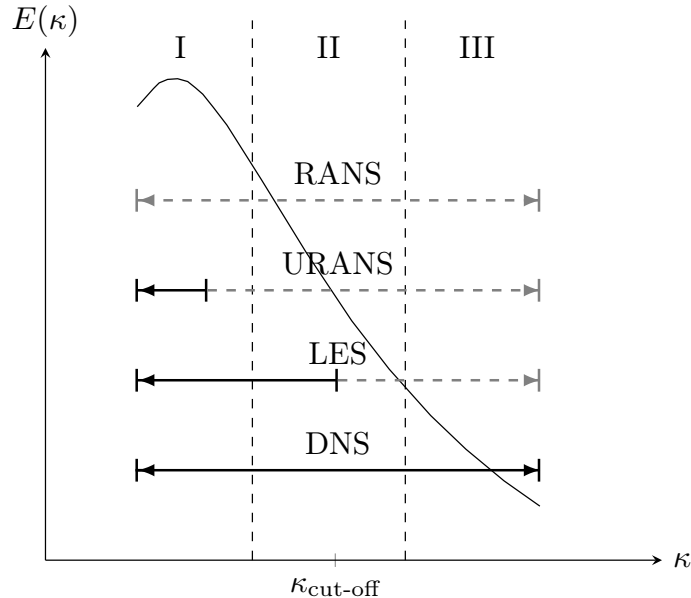


Figure 2.2: *Energy spectrum showing the scales at which different computational models resolve (-) and model (- -) turbulence.*

In contrast, the LES model is based on the spatial filtering of the governing equations instead of the time-averaging method used in the (U)RANS models. Consequently, the behavior of smaller scales is modeled but that of larger scales is resolved. The computational grid determines the definition of small and large scales. The large scales are resolvable by the computational grid, where the lower limit is usually of a similar order of magnitude as few cells. Small scales are commonly described as being Sub-Grid-Scales (SGS), and the point at which turbulent behavior starts being modeled rather than resolved is referred to as the cut-off limit (see $\kappa_{\text{cut-off}}$ in Figure ??). According to Spalart [61], the cut-off limit is in the order of five cells. However, the eddies with wavelengths in the order of the cut-off limit are not very accurate as they lack the connection to the smaller scales. Instead, they are dominated by the modeled viscosity from the SGS model. An example of the large and small scales is shown in Figure 2.3, where the dashed-line curve represents an SGS, whereas the whole-line represents what could be the lower limit for the larger scales.

The time-step in LES simulations should be significantly smaller compared to URANS simulations and is determined by the time scale of the smallest resolved scale. Additionally, higher spatial resolution is needed in all directions for the LES method compared to (U)RANS simulations, which only need relatively small cells in wall-normal directions.

For DNS simulations, the whole turbulence spectrum is resolved. However, this is very expensive and is not practical for high Reynolds number flows with complicated geometries because the spatial and temporal resolutions are determined by the Kolmogorov

length and time scales (the smallest scales from section III in Figure 2.1), respectively, necessitating the use of a even finer computational grids and smaller time-steps compared to LES.

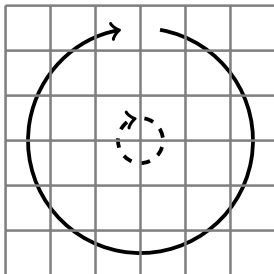


Figure 2.3: Modeled (- -) and resolved (-) scales.

2.3 URANS

Ensemble-averaging the governing equations has proven to be quite successful. For an arbitrary variable ϕ the averaging is expressed as

$$\bar{\phi} = \lim_{N \rightarrow \infty} \frac{1}{N} \sum_{i=1}^N \phi_i, \quad \phi = \bar{\phi} + \phi' \quad (2.7)$$

where ϕ' denotes the fluctuating part of ϕ . However, by ensemble-averaging the compressible form of the Navier-Stokes equations additional unknown terms, compared to the incompressible form, must be modelled. To avoid those extra terms, a density weighted average procedure (Favre-averaging [23]) is often used on top of the ensemble-averaging. The Favre-averaging of a flow variable ϕ is defined as

$$\hat{\phi} = \frac{\overline{\rho\phi}}{\bar{\rho}} \quad (2.8)$$

and the decomposition of instantaneous flow properties reads

$$\phi = \hat{\phi} + \phi'' = \frac{\overline{\rho\phi}}{\bar{\rho}} + \phi'' \quad (2.9)$$

where the ϕ'' term represents the combination of the Reynolds decomposition fluctuating component ϕ' and the density fluctuations. The term $\bar{\phi}$ is the mean component of a specific variable. $\hat{\phi}$ can be thought of as the low frequency component whereas ϕ'' represents high frequency one. Applying the Favre-averaging method in a combination to

the ensemble-averaging on the governing equations

$$\begin{aligned}
\frac{\partial \bar{\rho}}{\partial t} + \frac{\partial (\bar{\rho} \hat{u}_j)}{\partial x_j} &= 0 \\
\frac{\partial (\bar{\rho} \hat{u}_i)}{\partial t} + \frac{\partial (\bar{\rho} \hat{u}_i \hat{u}_j)}{\partial x_j} &= -\frac{\partial \bar{p} \delta_{ij}}{\partial x_i} + \frac{\partial \bar{\sigma}_{ij}}{\partial x_i} + \frac{\partial \tau_{ij}}{\partial x_j} \\
\frac{\partial (\bar{\rho} \hat{e}_0)}{\partial t} + \frac{\partial (\bar{\rho} \hat{e}_0 \hat{u}_j)}{\partial x_j} &= -\frac{\partial \bar{p} \hat{u}_j}{\partial x_j} + \frac{\partial}{\partial x_j} \left(C_p \frac{\mu}{Pr} \frac{\partial \hat{T}}{\partial x_j} + q_j^t \right) + \frac{\partial}{\partial x_j} (\hat{u}_i (\bar{\sigma}_{ij} + \tau_{ij})) \\
&\quad - \frac{1}{2} \frac{\partial}{\partial x_j} \bar{\rho} (\widehat{u_i u_i u_j} - \widehat{u_i u_i} \hat{u}_j)
\end{aligned} \tag{2.10}$$

where $\bar{\sigma}_{ij}$ is the Favre-averaged viscous stress tensor

$$\bar{\sigma}_{ij} = \mu \left(2 \hat{S}_{ij} - \frac{2}{3} \hat{S}_{mm} \delta_{ij} \right), \tag{2.11}$$

and \hat{S}_{ij} is the Favre-averaged strain rate tensor

$$\hat{S}_{ij} = \frac{1}{2} \left(\frac{\partial \hat{u}_i}{\partial x_j} + \frac{\partial \hat{u}_j}{\partial x_i} \right) \tag{2.12}$$

It is immediately apparent that the Favre-averaged equations (Eqns. 2.10) are very similar to the original Navier-Stokes equations (Eqns. 2.1).

To solve this system of equations, there are three unknowns. The triple velocity correlation term in the energy equation is neglected, leaving two additional terms - one for the turbulent stresses and one for the heat flux. The turbulent stress term, including the density,

$$\begin{aligned}
\tau_{ij} &= -\bar{\rho} (\widehat{u_i u_j} - \hat{u}_i \hat{u}_j) \\
&= -\bar{\rho} \left(\underbrace{(\widehat{u_i u_j} - \hat{u}_i \hat{u}_j)}_I + \underbrace{(\widehat{u_i'' u_j} + \widehat{u_i u_j''})}_{II} + \underbrace{\widehat{u_i'' u_j''}}_{III} \right)
\end{aligned} \tag{2.13}$$

consists of three different terms - the Leonard stresses term *I*, the cross stresses term *II*, and the Reynolds stresses term *III*. The turbulent heat flux is given by

$$q_j^t = -C_p \bar{\rho} (\widehat{T u_j} - \hat{T} \hat{u}_j) \tag{2.14}$$

This means that the closed set of equations formed by the Navier-Stokes equations is almost but not completely enclosed by the averaging technique, and the unknown turbulent terms must be modeled.

To evaluate the turbulent stress term and thereby close the set of equations, additional transport equations known as turbulence models are introduced. These equations solve for one or more new variables. Many different models exist, where the most common procedure is to use the Boussinesq closure. An eddy viscosity (ν_t) is introduced to relate

the turbulence stresses to the mean flow properties to close the system of equations, where the turbulent shear stress is proportional to the rate of mean strain:

$$-\tau_{ij} = -\widehat{u'_i u'_j} = \nu_t 2\hat{S}_{ij} - \frac{2}{3}k\delta_{ij} \quad (2.15)$$

and the turbulent heat flux is modeled as a diffusion term

$$q_j^t = C_p \frac{\mu_t}{Pr_t} \frac{\partial \hat{T}}{\partial x_j} \quad (2.16)$$

Examples of such models are the $k - \omega$ Shear Stress Transport (SST) two-equation model [42] and the Spalart and Allmaras one equation model (SA) [62]. Throughout the extent of this thesis, the RANS and URANS results are modeled using the SST model for the CFX simulations and the SA model for G3D::Flow simulations.

The SA turbulence model is presented for completion and because the SA model was implemented into G3D::Flow. The single equation turbulence model assumes that the turbulent stress tensor is given by the expression

$$\tau_{ij} = -2\nu_t \hat{S}_{ij} \quad (2.17)$$

The SA model solves for a new turbulence variable, $\tilde{\nu}$. The conservative and compressible form of the model (without the f_{t1} trip term) is as follows [62, 63]:

$$\begin{aligned} \frac{\partial \bar{\rho} \tilde{\nu}}{\partial t} + \frac{\partial}{\partial x_j} (\bar{\rho} u_i u_j) &= \tilde{S} \tilde{\nu} (1 - f_{t2}) c_{b1} \bar{\rho} + \frac{1}{\sigma} \frac{\partial}{\partial x_j} \left(\bar{\rho} (\nu + \tilde{\nu}) \frac{\partial \tilde{\nu}}{\partial x_j} \right) \\ + \frac{c_{b2}}{\sigma} \bar{\rho} \left(\frac{\partial \tilde{\nu}}{\partial x_j} \right)^2 &- \bar{\rho} \left(c_{w1} f_w - \frac{c_{b1}}{\kappa^2} f_{t2} \right) \left(\frac{\tilde{\nu}}{d} \right)^2 + \frac{1}{\sigma} (\nu + \tilde{\nu}) \frac{\partial \bar{\rho}}{\partial x_j} \frac{\partial \tilde{\nu}}{\partial x_j} \end{aligned} \quad (2.18)$$

where

$$\begin{aligned} \nu_t &= \tilde{\nu} f_{v1}, & f_{v1} &= \frac{\chi^3}{\chi^3 + c_{v1}^3}, & \chi &= \frac{\tilde{\nu}}{\nu} \\ \tilde{S} &= S + \frac{\tilde{\nu}}{\kappa^2 d^2} f_{v2}, & f_{v2} &= 1 - \frac{\chi}{1 + \chi f_{v1}} \\ f_w &= g \left(\frac{1 + c_{w3}^6}{g^6 + c_{w3}^6} \right)^{1/6}, & g &= r + c_{w2} (r^6 - r), & r &= \frac{\tilde{\nu}}{\tilde{S} \kappa^2 d^2} \\ f_{t2} &= c_{t3} \exp(-c_{t4} \chi^2) \end{aligned} \quad (2.19)$$

and the corresponding constants are

$$\begin{aligned} c_{b1} &= 0.1355, & \sigma &= 2/3, & c_{b2} &= 0.622, & \kappa &= 0.41, \\ c_{w2} &= 0.3, & c_{w3} &= 2, & c_{v1} &= 7.1, & c_{t3} &= 1.2, \\ c_{t4} &= 0.5, & c_{w1} &= c_{b1}/\kappa^2 + (1 + c_{b2})/\sigma. \end{aligned} \quad (2.20)$$

In the SA model, the turbulence stress term τ_{ij} (referred to as the Reynolds stress term in RANS models) accounts for the effects of the entire energy spectrum over all length scales in the average flow field. This means that all turbulence is modeled.

2.4 LES

The LES equations are written in the same way as the governing equations of URANS except, instead of applying ensemble-averaging, spatial filtering is used. Applying a spatial filtering on an arbitrary variable ϕ in 1D, yields

$$\bar{\phi}(x, t) = \frac{1}{\Delta x} \int_{x-0.5\Delta x}^{x+0.5\Delta x} \phi(\xi, t) d\xi, \quad \phi = \bar{\phi} + \phi' \quad (2.21)$$

Eqns. 2.10-2.14 can be regarded as the Favre-averaged LES governing equations, with the modification that (\bullet) represents spatial filtering instead of ensemble-averaging. Furthermore, because a finite volume discretisation is used, the local control volume is based on the computational grid and represents the spatial filtering (*i.e.* an implicit filter is used). LES models describe turbulent stresses in a different way compared to RANS. The stresses that are not resolved are modeled using SGS models, the simplest of which is the zero-equation Smagorinsky model [59]:

$$\begin{aligned} \tau_{ij} - \frac{1}{3}\delta_{ij}\tau_{kk} &= -\nu_{sgs} \left(\frac{\partial \bar{u}_i}{\partial x_j} + \frac{\partial \bar{u}_j}{\partial x_i} \right) = -2\nu_{sgs}\bar{S}_{ij} \\ \nu_{sgs} &= (C_S\Delta)^2 \sqrt{2\bar{S}_{ij}\bar{S}_{ij}} \equiv (C_S\Delta) |\bar{S}| \end{aligned} \quad (2.22)$$

Additionally, the filter-width is defined as the local grid size:

$$\Delta = (\Delta V_{IJK})^{1/3} \quad (2.23)$$

This means that the main difference between RANS and LES is the extent to which the Reynolds stresses are resolved (the whole energy spectrum is modeled in RANS).

As described in the previous section, the SGS is defined by the cut-off wavelength, *i.e.* length-scales below the cut-off are modeled, whereas those above are resolved. Consequently, the use of finer meshes reduces the proportion of the energy spectrum that is modeled, which can make common grid-dependency studies difficult. Furthermore, LES simulations are quite computationally demanding because the larger scales become quite small in the vicinity of walls, necessitating the use of a fine mesh and a small time-step.

2.5 Hybrid RANS/LES

The preceding sections describe the URANS and LES formulations. A class of hybrid turbulence modeling technique, known as hybrid RANS/LES methods, have recently been introduced to combine the best aspects of the URANS and LES approaches. The hybrid models simulate certain regions (typically, attached or mildly separated boundary layers) using the URANS formulation of the governing equations, whereas the free-stream region and well-separated areas are solved using LES. The transition between URANS and LES can be predefined (using zonal methods) or calculated as a part of the model. This means that the boundary layer, for which URANS models have proven quite reliable, can use a relatively coarse mesh, substantially reducing computational costs as fewer cells

and a larger time-step can be used. In wall-bounded LES simulations, up to 90% of the total number of cells can be needed in the boundary layers. Using the LES model in the free-stream means that transient flow features of the main flow are captured.

Figure 2.4 shows a schematic view of a hypothetical inclined flat plate simulation using a hybrid modeling technique. In the figure, the free-stream and the separated region on the suction side are simulated using LES, whereas the attached boundary layer at the pressure side is simulated using URANS.

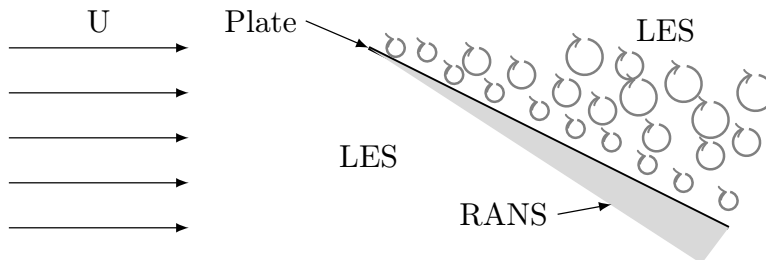


Figure 2.4: *An inclined flat plate simulated with a hybrid RANS/LES model.*

There are several methods available, where the most well-known is the Detached Eddy Simulation (DES) family of models. Two different hybrid models are used throughout this thesis. In CFX, the Stress Blended Eddy Simulation (SBES) model is used, whereas a version of the DES model was implemented and used in G3D::Flow.

2.5.1 DDES

The hybrid RANS/LES model, Delayed Detached Eddy Simulation model (DDES) [64], is based on the original DES model [65]. The version implemented into G3D::Flow uses the SA one-equation turbulence model in URANS mode and as an SGS model in the LES region. To implement the SA model as an SGS model, the length scale in the destruction term (Eq. 2.18) was modified to account for the change from RANS to LES. For the SA model, the wall distance was replaced with a different length scale, as shown in Eq. 2.27. In other words, the wall distance, d , in Eqns. 2.18 and 2.19 is replaced by \tilde{d} in Eq. 2.27. DDES is an improvement over the original DES model because the switching between LES and RANS is governed by both the cell size and the flow. This has great benefits because the original DES model had a high risk of premature switching from RANS to LES for grids with a stream-wise grid spacing similar in size to the boundary layer thickness. Such premature switching causes grid-induced separation [64], which has particularly severe effects in simulations of flows with strong gradients in the stream-wise direction. The grid-induced separation, is caused by the DES model extending the LES region into the boundary layer, where the grid is not fine enough to resolve the turbulent stresses. This problem was addressed in the DDES model by adding a shielding function that prevents the application of the LES formulation inside the boundary layers. The shielding function,

$$f_d = 1 - \tanh [(8r_d)^3]. \quad (2.24)$$

is designed to be 0 inside the boundary layer but 1 outside it. The function r_d is similar to the r function in the SA model [62]

$$r_d = \frac{\nu + \nu_t}{\sqrt{U_{i,j}U_{i,j}}\kappa^2 d^2} \quad (2.25)$$

The length scale introduced in the original DES model was based only on the wall distance and the grid spacing Δ

$$\tilde{d} = \min(d, C_{DES}\Delta) \quad (2.26)$$

However, as noted above, this can cause grid-induced separation. To eliminate this problem, the DDES model uses a modified length scale, incorporating a boundary layer shielding function, f_d

$$\tilde{d} = d - f_d \max(0, d - C_{DES}\Delta). \quad (2.27)$$

When $f_d = 0$, the model behaves like a URANS model, but when $f_d = 1$, it behaves like the original DES model shown in Eq. (2.26). Furthermore, the DES model should be in LES mode outside the boundary layer.

Shur et al. [50] compared the performance of the original DES model to experimental results, using the SA model to describe the SGS behavior. Good achievement with experimental data was achieved when simulating isotropic turbulence using a filtering factor value of $C_{DES} = 0.65$.

The coefficients of the f_d function were calibrated using a flat-plate boundary layer, but recent studies have shown that some modifications may be necessary for good performance simulating specific problems. For example, Ashton [9] encountered problems with the shielding function during studies on a three-element airfoil. It was concluded that these problems were due to excessively fine stream-wise and span-wise grid sizes, even though the DDES model was used. The small cells subjected to strong stream-wise pressure gradients, over curved surfaces, caused the shielding function to break down, allowing the LES model to be applied inside the boundary layer. Probst et al. [48] encountered a similar problem in studies on a simple airfoil. In their opinion, a coarser mesh was not a viable option because a high resolution in the stream-wise direction was required to capture the adverse pressure gradient over the wing. Instead, they suggested a modification to the f_d function where the coefficient in front of r_d was increased from 8 to 16, as shown in Eq. 2.28.

$$f_d = 1 - \tanh [(16r_d)^3]. \quad (2.28)$$

The above discussion, shows that despite the modifications to allow the DDES model to cope with ambiguous grids, the solutions remain sensitive to the stream-wise grid spacing.

Additionally, it has been shown that when using the SA model as a base model for DDES, f_{t2} should be excluded in the equations because it increases the possibility of a laminar boundary layer on fine grids [73]. Excluding the f_{t2} term is usually referred to as the SA-noft2 model [35].

2.5.2 ANSYS SBES

The hybrid RANS/LES model, SBES, is used as it has proven to be successful in protecting the boundary layer, even on grids with fine stream-wise cell-sizes [41] (a problem with

DDES, discussed above). The SST model is used in the URANS regions, whereas in the LES regions, the SGS is modeled using the WALE algebraic model [46]. The idea behind the SBES model is to explicitly change between LES and URANS, using a shielding function, f_s . When both the URANS and SGS models are eddy-viscosity based models the SBES model's eddy-viscosity is defined as

$$\nu_t^{SBES} = f_s \cdot \nu_t^{RANS} + (1 - f_s) \cdot \nu_t^{LES} \quad (2.29)$$

where f_s is the previously mentioned shielding function, designed to protect the boundary layer from being solved in LES mode. This function is unpublished and proprietary to ANSYS. It is not ideal to use a function that can be considered as a "black box" but the performance of the model has been validated for various test cases [41] and therefore, it is considered as a practical option.

2.6 Spatial discretisation

The scale-resolving model, in this case the LES model, dissipates the energy from the turbulence spectrum at the grid resolution limit, assuming that all the energy is dissipated through the LES model. This means that the numerical scheme is assumed to be non-dissipative. Therefore, when performing LES, a low-dissipation scheme has to be utilized (low, relative to the dissipation provided by the SGS LES model). Pure central differencing (CD), which is a low dissipation scheme, has been proven to be unstable and result in nonphysical flow features when used for industrial simulations performed with non-ideal grids [19, 43]. Therefore, two spatial discretization methods are used for different solves:

- CFX - Bounded Central-Differencing, which switches between the CD and second-order upwind schemes, dependent on the flow [41].
- G3D::Flow - Third-Order-Upwind-Low-Dissipation is used, which ensures a small amount of up-winding, increasing the numerical stability, compared to the CD scheme [40].

For both solvers, it is sufficient to use first-order spatial discretization for the turbulence model convective terms as the source terms govern those equations.

Chapter 3

Acceleration Techniques

G3D::Flow is an explicit CFD solver where the solution is advanced using a 3-stage Runge-Kutta (RK) scheme. Explicitly solving the time-accurate governing equations limits the allowed physical time-step, where the limitation is due to numerical stability. Instead, it is preferred that physics would limit time-steps.

The governing equations 2.1 can be written on a compact form

$$\frac{\partial Q}{\partial t} = R \quad (3.1)$$

where

$$Q = [\rho, \rho u, \rho v, \rho w, \rho e_0]^T \quad (3.2)$$

and R represents the spatial residual. Jameson [34] introduced a methodology where an explicit RK multistage scheme was accelerated using a pseudo time (τ). The idea was to implement sub-iterations, integrated into the normal iteration process, to allow for larger physical time-steps with the means of steady-state acceleration techniques. A source term was added to Eq. 3.1, which accounts for the marching in the pseudo-time-step

$$\frac{\partial Q}{\partial \tau} = R - \frac{\partial Q}{\partial t} = R^* \quad (3.3)$$

where τ is the fictitious time and R^* is the new residual when advancing in τ . Because of the co-existence of two uncoupled times, the method is usually referred to as a Dual time-stepping (DT) method. As for the normal spatial residual R , when performing steady-state simulations, the new R^* residual approaches zero when marching in pseudo time. This is a key factor when applying steady-state convergence acceleration techniques. Therefore, the steady-state acceleration techniques can be used on the inner iterations and still sustain the time-accuracy of the solution.

Breaking the pseudo time-step into an iterative process. It is common to solve Eq. 3.3 using multistage RK schemes

$$\begin{aligned} Q^{(0)} &= Q^l \\ Q^{(k+1)} &= Q^{(0)} + \alpha_k \Delta \tau R^*(Q^{(k)}) \\ &\vdots \\ Q^{l+1} &= Q^{(k+1)} \end{aligned} \quad (3.4)$$

where k represents the RK stage and l inner-iterations in pseudo time. Furthermore, for second order accuracy, the physical time derivative is discretised using second order backward Euler

$$\frac{\partial Q}{\partial t} = \frac{3Q^{n+1} - 4Q^n + Q^{n-1}}{2\Delta t} \quad (3.5)$$

where the n represents the current physical time step, $n - 1$ the previous one and $n + 1$ the next time step. Rewriting the DT residual for the state vector at $t = n$

$$R^*(Q^{(n)}) = R - \frac{3Q^{n+1} - 4Q^n + Q^{n-1}}{2\Delta t} \quad (3.6)$$

Now, the k -th stage of the RK step can be expanded, where the unknown $l + 1$ is replaced with $k + 1$

$$Q^{(k+1)} = Q^{(0)} + \alpha_k \Delta \tau \left(R^k - \frac{3Q^{k+1} - 4Q^n + Q^{n-1}}{2\Delta t} \right) \quad (3.7)$$

isolating all $k + 1$ terms on the left-hand-side

$$Q^{(k+1)}(1 + 3/2\alpha_k \Delta \tau) = Q^{(0)} + \alpha_k \Delta \tau \left(R^k - \frac{-4Q^n + Q^{n-1}}{2\Delta t} \right) \quad (3.8)$$

All terms on the right-hand-side are known and each RK stage inside the DT iterations can be calculated as

$$Q^{(k+1)} = Q^{(0)} + \frac{\alpha_k \Delta \tau}{1 + 3/2\alpha_k \Delta \tau} \left\{ R^k - \frac{3Q^{(0)} - 4Q^n + Q^{n-1}}{2\Delta t} \right\} \quad (3.9)$$

The inner iterations are considered converged when $Q^{l+1} \approx Q^l$ from Eq. 3.4.

A 5-stage RK scheme was implemented into G3D::Flow to solve the pseudo time derivative. The α coefficients are given by [68]

$$[\alpha_1, \dots, \alpha_5] = [0.25, 0.1667, 0.375, 0.5, 1.0] \quad (3.10)$$

To improve the convergence of the sub-iterations local time-stepping, Implicit Residual Smoothing (IRSM) and low-speed preconditioning can be applied to the residuals without compromising the time-accuracy of the solution.

Local time-stepping

Local time-stepping indicates that the governing equations (Eqns. 3.1 and 2.1) are integrated using the largest allowed time-step for each computational cell. Therefore, each computational cell will have individual time-steps. This will accelerate the steady-state convergence considerable but the time accuracy of the solution is broken. As discussed in the previous section, applying the local time-stepping method on the inner iterations for the DT method sustains the time-accuracy.

Implicit residual smoothing

In general, Runge-Kutta methods, like the one presented in Eq. 3.4, have an upper limit on the allowed time-step. For G3D::Flow, the upper limit is $CFL = 1.2$ for the 3-stage

RK in the explicit solver. However, for the 5-stage RK, in the DT solver, the upper limit is $CFL = 3.75$. Jameson and Baker [33] introduced an IRSM technique, with the objective to increase the stability range, and thus achieve faster convergence with larger time-steps. Furthermore, the IRSM dampens out the high-frequency error components of the residual. An IRSM was implemented into G3D::Flow, where smoothing is performed on the term inside the curly brackets on the right-hand-side of Eq. 3.9. The smoothing is performed for each Runge-Kutta stage, before updating Q^{k+1} . Since the value of inside the parenthesis approached zero when the sub-iterations converge, the solution will be time-accurate.

It is common practice to smooth the residuals in each grid direction at a time [11]:

$$\begin{aligned}
-\epsilon^I R_{I-1,J,K}^* + (1 + 2\epsilon^I) R_{I,J,K}^* - \epsilon^I R_{I+1,J,K}^* &= R_{I,J,K} \\
-\epsilon^J R_{I,J-1,K}^{**} + (1 + 2\epsilon^J) R_{I,J,K}^{**} - \epsilon^J R_{I,J+1,K}^{**} &= R_{I,J,K} \\
-\epsilon^K R_{I,J,K-1}^{***} + (1 + 2\epsilon^K) R_{I,J,K}^{***} - \epsilon^K R_{I,J,K+1}^{***} &= R_{I,J,K}
\end{aligned} \tag{3.11}$$

where $R_{I,J,K}^*$, $R_{I,J,K}^{**}$ and $R_{I,J,K}^{***}$ represent the smoothed residuals in I-, J- and K-grid directions, respectively. $R_{I,J,K}$ is the unsmoothed residual. Due to convenience the IRSM in G3D::Flow is performed in all directions for a specific cell, instead of smoothing in separate directions. The smoothing coefficients, ϵ^I , ϵ^J and ϵ^K , are calculated for individual cells to provide the optimum amount of smoothing. It is common to define the coefficients as a function of the spectral radii of the convective flux Jacobians. However, as a result, the coefficients have to be calculated for each iteration, increasing the computational cost. Therefore, an approach is taken where the smoothing coefficients are a function off the cell-aspect ratio (AR) [67, 68, 11]

$$\epsilon = \max \left\{ \frac{1}{4} \left[\left(\frac{CFL}{CFL^*} \frac{1}{(1 + \psi AR)} \right)^2 - 1 \right], 0 \right\} \tag{3.12}$$

where the CFL^* is the stability limit of the unsmoothed scheme, CFL is specified for each simulation (usually around $2 \cdot CFL^*$) and ψ is a calibrated parameter. A conservative value for 2D simulations is $\psi^{2D} = 0.11$ [67]. For 3D simulations $\psi^{3D} = \psi^{2D}/2 = 0.055$. Additionally, the AR is dependant on the dimension of the simulation where in the x-direction $AR_x^{2D} = h_x/h_y$ and $AR_x^{3D} = h_x/(h_y + h_z)$.

The pseudo time-step can be calculated from each of the cells in the computational domain. However, stability problems can arise when the pseudo time-step (τ) is larger than the physical one (t). This can happen in viscous simulations where the cells in the free-stream are generally much larger compared to the ones located in boundary layers. A linear stability analysis result in a correction to the pseudo time-step [8]

$$\Delta\tau = \min \left(\Delta\tau, \frac{\Delta t}{3/2(CFL/CFL^*)} \right) \tag{3.13}$$

Low-speed preconditioning

Compressible flow solvers are ill-conditioned for low-speed flow regimes. That is because the convective terms of the governing equations 3.1 become stiff. The stiffness can be

determined by the characteristic condition number which is defined as the ratio between the largest and smallest eigenvalues

$$C = \frac{|(\Lambda_c)_{\max}|}{|(\Lambda_c)_{\min}|} \quad (3.14)$$

For a 3D case, there are five eigenvalues:

$$\begin{aligned} (\Lambda_c)_{1-3} &= V && \text{(convective modes)} \\ (\Lambda_c)_{4,5} &= V \pm c && \text{(acoustic modes)} \end{aligned} \quad (3.15)$$

where V is the contravariant velocity and c is the speed of sound. Equation 3.14 can therefore be rewritten

$$C = \frac{|(\Lambda_c)_{\max}|}{|(\Lambda_c)_{\min}|} = \frac{|V| + c}{|V|} = \frac{M + 1}{M} \quad (3.16)$$

For subsonic flows, the stiffness increases when the velocity approaches zero. Furthermore, the local time-step is limited by the largest eigenvalue. This means that the increased stiffness results in slow propagation of slowest moving wave (lowest eigenvalue) decreasing the convergence rate to a steady state solution. A low-speed preconditioner is a method to scale the eigenvalues to improve the convection of the slowest waves.

Erikson [21] implemented a low-speed preconditioning into the precursor of G3D::Flow, which was then implemented into G3D::Flow. There, the preconditioning is applied on the governing equations. On conservative form the preconditioned governing equations become

$$P_c^{-1} \frac{\partial Q}{\partial t} = R^* \quad (3.17)$$

where P is the preconditioning matrix. On primitive form, for 2D and in-viscid flow

$$P_0 = \begin{bmatrix} 1 & 0 & 0 & -\frac{(1-\alpha)}{c^2} \\ 0 & 1 & 0 & 0 \\ 0 & 0 & 1 & 0 \\ 0 & 0 & 0 & \alpha \end{bmatrix} \quad (3.18)$$

The relation between the preconditioning for the conservative (Q) and primitive (Q_0) variables is $P_c = \frac{\partial Q}{\partial Q_0} P_0 \frac{\partial Q_0}{\partial Q}$. Now consider dual time-stepping equation (Eq. 3.3), where a low-speed preconditioner is applied on the pseudo time-derivative. This is done to ensure the time-accuracy of the solution since the pseudo time-derivative approaches zero with increased number of sub-iterations.

$$P_c^{-1} \frac{\partial Q}{\partial \tau} = R^* \quad (3.19)$$

Following the same procedure as before but now with the preconditioning applied

$$Q^{(k+1)} = Q^{(0)} + \frac{\alpha_k \Delta \tau P_c}{I + 3/2 \alpha_k \Delta \tau P_c} \left\{ R^k - \frac{3Q^{(0)} - 4Q^n + Q^{n-1}}{2\Delta t} \right\} \quad (3.20)$$

The main difference between Eq. 3.9 and Eq. 3.20 is the matrix in the denominator. The matrix in the denominator causes a cumbersome calculation but the procedure from Turkel and Vatsa [72, 71] is followed. For an arbitrary vector \vec{x}

$$\begin{aligned} P_c \vec{x} &= \vec{x} + (\alpha - 1)y_1 \vec{z} \\ (I + d \cdot P_c)^{-1} \vec{x} &= \frac{\vec{x} + ey_1 \vec{z}}{1 + d} \end{aligned} \quad (3.21)$$

where

$$\begin{aligned} y_1 &= \frac{\gamma - 1}{c^2} \left[\frac{q^2}{2} x_1 - (ux_2 + vx_3) + x_5 \right] \\ \vec{z} &= [1, u, v, h]^T \\ c^2 &= \frac{\gamma p}{\rho}, \quad q^2 = u^2 + v^2, \quad h = \frac{c^2}{\gamma - 1} + \frac{q^2}{2}, \quad d = \alpha_k 3/2 \frac{\Delta \tau}{\Delta t} \end{aligned} \quad (3.22)$$

c is the speed of sound, γ is the heat capacity ratio, u and v velocities in x and y , respectively, p is the pressure, ρ is the density, k is the Runge-Kutta stage coefficient and 3/2 is related to which temporal discretisation is used for the physical time-step (3/2 because of the second-order backward Euler).

Combining Eqns. 3.20 and 3.21, the time-accurate solution can be calculated using dual time-stepping and accelerated with local time-steps, IRSM and low-speed preconditioning.

3.1 Verification

To verify the implementations into G3D::Flow, several tests were done.

In-viscid 2D flow with prescribed periodic inlet disturbance is simulated. The rectangular grid is presented in Figure 3.1. First, a steady-state solution is obtained where the flow is oriented in x-direction. The flow is disturbed in the y-direction with a sinusoidal wave. Two points are monitored, one on the left boundary (the inlet) and another in the center of the domain.

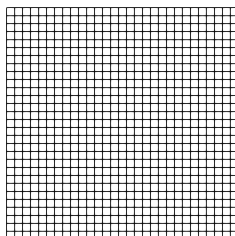


Figure 3.1: *Rectangular grid.*

Figures 3.2a and 3.2b show the y-velocity at the inlet and the middle of the domain, respectively. The sinusoidal wave is convected with constant u-velocity, explaining the zero v-velocity in the middle of the domain for the first 0.02s. The results are achieved using

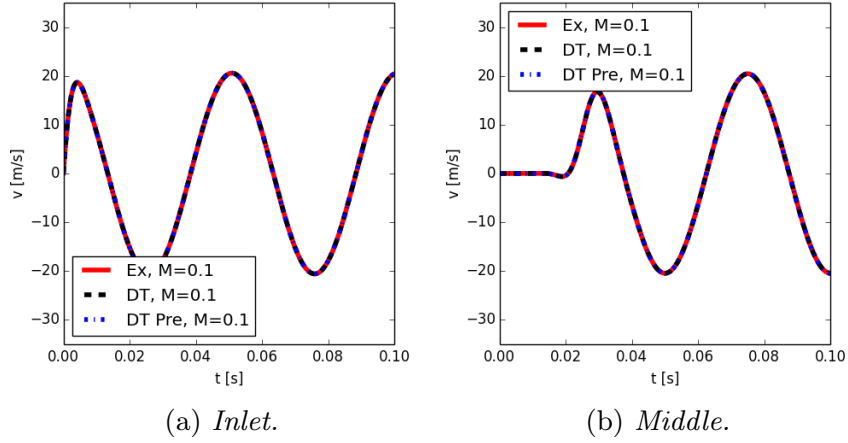


Figure 3.2: *y-velocity component.*

explicit and dual time-stepping methods. Furthermore, for the dual time-stepping method, simulations were performed with and without the low-speed preconditioning, where the IRSM and local time-stepping are used for the inner iterations. The time-step was kept the same in both simulations to validate the implementation of the dual time-stepping method. The Mach number of the x-component of the velocity is $M = 0.1$. Both methods show identical velocity behavior, as they should. Furthermore, viscous simulations were performed to verify the generality of the rectangular configuration, with the same results.

2D cylinder cases ($D_{Re=185} = 0.01$ & $D_{Re=740} = 0.04$) were simulated using the explicit and the dual time-stepping solvers. Figure 3.3 presents the computational domain with 321 cells in the circumferential direction and 281 cells in the wall normal direction. The outlet boundaries are specified with free-stream Mach-number, $M = 0.2$. Table 3.1 shows

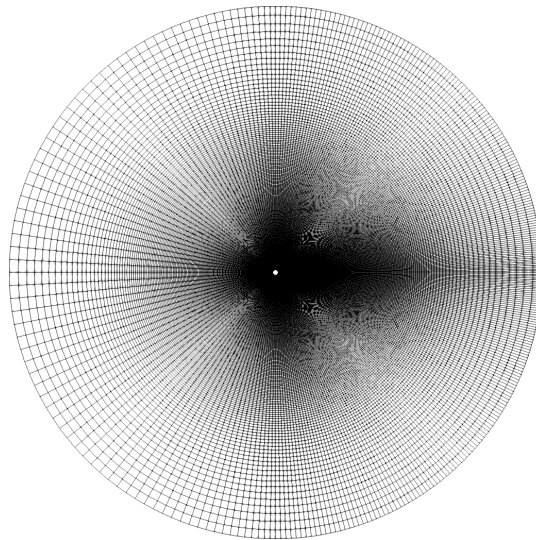


Figure 3.3: *Cylinder grid.*

the time-averaged lift and drag coefficients (Eq. 3.23), and Strouhal number, averaged over 4s for two different Reynolds numbers. The lower Reynolds number lies in the laminar regime, whereas the higher one is in the turbulent regime. Different Reynolds numbers are obtained by increasing the diameter for the cylinder. For both Reynolds numbers, the difference between the two solvers is negligible. Furthermore, the physical time-step for the DT simulations was 100 times larger compared to the explicit calculations. For both the cases, the effective simulation acceleration was ≈ 5 (each inner-iteration is relatively expensive compared to the explicit iteration as the 5-stage RK, the IRSM and the low-speed preconditioning add to the computational cost).

Table 3.1: Cylinder.

Solver	Re	C_L	C_D	St
Explicit	$Re = 185$	-0.015	0.678	0.190
DT	$Re = 185$	0.020	0.677	0.189
Explicit	$Re = 740$	-0.018	2.72	0.216
DT	$Re = 740$	0.005	2.74	0.216

$$C_L = \frac{2L}{\rho u^2 D} \quad C_D = \frac{2D}{\rho u^2 D} \quad (3.23)$$

For the two verification cases, the implemented dual time-stepping solver was successful in reproducing the solution obtained with the already verified explicit solver. Additionally, a significant acceleration was obtained for the DT solver.

Chapter 4

Retrospective view

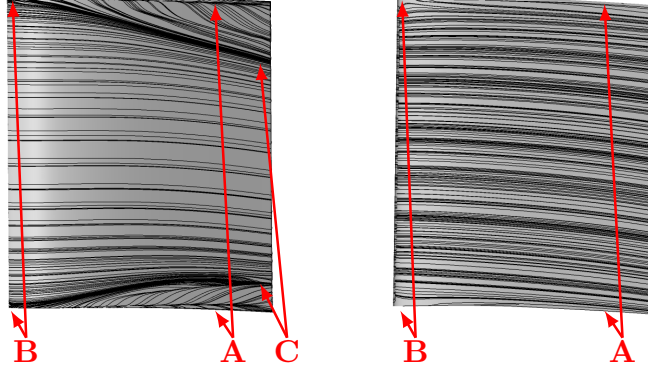
An important part of the Ph.D. study is to develop understanding and knowledge of the subject, which for this thesis is the integrated ICD. Therefore, it is of interest to revisit the publications written in early stages with the knowledge gained during the Ph.D. process. In this chapter, a retrospective view is provided on the early papers where the internal flow field of an ICD was discussed (Paper B, Paper D and Paper E). The extended discussion and analysis are based on the results from papers F and G.

4.1 Pre-swirler

4.1.1 Horseshoe vortex

The discussion related to the flow across the Pre-swirler (PSW) blades concluded that the blades generate vortices that interact with the downstream components (Figures 11 in Paper A, 12-13 in Paper B, 8 and 12 in Paper D, and 9a) and 12 in Paper F). However, the origin of those vortices was never verified. The PSW represents a stationary blade row located upstream of the duct and emulates the last rotor of the LPC by turning the flow. The relatively simple blade profile and steady inlet flow conditions result in rather complex secondary flow structures. The secondary flow structures have been studied by many authors where, for example, Sharma and Butlet [49] presented a method to estimate the losses caused by secondary flow features and end-walls. Langston [37] presented a literature survey where a detailed discussion was given on the secondary flow structures in an axial flow turbine cascade. Even though both papers presented analysis for turbine cascades, the same behavior can be found for the PSW. Consider a single blade as discussed by Langston [37]. The flow will hit the leading edge of the blade, resulting in a stagnation line, where the pressure reaches a local maximum. The pressure at the stagnation line is proportional to the dynamic pressure. At the intersection between the blade and the end-walls (both the inner and outer casing), the stagnation pressure is lower, due to lower inlet velocity inside the end-walls boundary layers, causing an outwards circulation or a vortex. The vortex is commonly referred to as a horseshoe vortex. The horseshoe vortex is divided into two main components, pressure and suction side vortex, which are rotating clockwise and counter-clockwise, respectively. Due to the pressure difference between two different blades, the pressure side horseshoe vortex transforms into a passage vortex when it is dragged from the pressure side of one blade to the suction side of an adjacent blade. The passage vortex increases in magnitude through the blade passage and interacts with the suction side vortex. In Figure 4.1, the horseshoe vortex can be identified. At the suction surface (Figure 4.1a), the horseshoe vortex is visible at the leading edge (B), upstream of the mixing with the passage vortex. Downstream of the mixing, the passage vortex is observed to increase in magnitude (reaching further into the flow-path, C). A small corner vortex is observed near the end-walls on both the suction and pressure sides (A). The secondary flow behavior is further verified by considering the

hub streamlines (Figure 4.2), where a saddle point (**S**) is identified upstream of the blades and the flow is transported from the pressure side to the suction side (**P**). Additionally, the corner vortex is visible at the suction side, near the trailing edge (**Co**). This system of vortex structures is the origin of the mechanism observed at the downstream FT evaluation surface (surface defined in Papers B, D, E and F).



(a) *Suction side (TE-LE)*. (b) *Pressure side (LE-TE)*.

Figure 4.1: *PSW blade streamlines*.

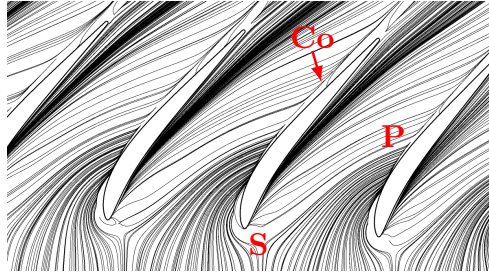


Figure 4.2: *PSW inner wall streamlines*.

4.1.2 PSW representing a rotor

Using a PSW instead of the LPC's last rotor simplifies both the experimental setup and the CFD simulations. The experimental setup is easier to control as no rotating components are used and the CFD simulations are not as computationally demanding as the true flow physics can be captured in a relatively short time-frame. As the main objective was to identify the interaction between the bleed flow and the ICD, the current configuration was sufficient. However, several interaction effects are not included when excluding the upstream rotor:

1. Effects from the bleed system, OGVs and strut's potential fields on the LPC's rotor.

The static pressure field is presented in Figure 13 in Paper F at an axial location close to where the rotor's trailing edge would be located. From the contours, it can be concluded that the rotor performance would be affected by the potential field (highest pressure

near the casing for 0% bleed but near mid-span for 40%). In order to quantify the effect, simulations where the rotor is included would be required. Karakasis et al. [36] showed that the potential field from the strut affected the rotor, resulting in a circumferential variation of the pressure field, locally increasing the rotor pressure.

2. Different rotor tip loading as a function of the bleed fraction.

From the same figure as previously mentioned (Figure 13 in Paper F), it is expected that the loading near the casing would be altered since the flow near the casing would be accelerated more with an increased bleed fraction.

3. Transient rotor wakes to interact with the downstream components.

This has been the subject of several papers where Karakasis et al. [36] concluded that the unsteady rotor effects would have a minimal impact on the performance of the downstream ICD. However, the rotor wakes would impact the performance of the OGVs. Whether it would have a positive or a negative impact remains unanswered in this thesis.

4.2 OGV

The OGV blades are integrated into the S-shaped duct, relatively close to the strut. The OGV blades have a 3D design to improve the aerodynamic performance [15], to limit the upstream potential field of the strut and matches the static pressure requirements of the bend [76].

The performance of the OGV blades is highly compromised when subjected to large amount of bleed. As discussed in Paper F, the axial momentum is extracted through the bleed pipe, whereas the tangential momentum is conserved. This behavior causes the incidence on the OGV blades to take drastic changes, where the upstream swirl is presented in Table 4.1 (data extracted from Figure 11b) in Paper F). The swirl increases by 22.5%, 15.9% and 36.4%, for the 10% and 40% bleed cases, at 10%, 50% and 90% span, respectively. The large difference for the upstream swirl, severely impacts the performance of the OGV blades.

Table 4.1: Swirl upstream of the OGVs [degrees] (Paper F).

SpanBleed	SST-0%	SST-10%	SST-30%	SST-40%
10%	35.5	37.2	40.1	43.5
50%	39.0	40.1	43.5	45.2
90%	43.1	45.7	54.7	58.8

The effect on the OGV performance can be further analyzed by considering the swirl downstream of the OGVs. The OGV blades are able to deliver similar swirl at mid-span (1.1° to 2.8° between 0% and 40% bleed), but the lowest amount of variation was observed for the OGV upstream swirl (Table 4.1). At 90% span, the OGV exit swirl is decreased significantly, from 2.3° for the 0% bleed to -5.7° for the 40% bleed. Near the hub, at 10% span, the swirl does not take drastic changes ($\Delta\text{Swirl}=1^\circ$). However, the boundary layer near the hub is thicker, both upstream and downstream of the OGV blades.

The relation between increase bleed and the hub boundary layer thickness was quantified in Paper G, Table 5 (all blades excluded). The displacement thickness (δ^*), downstream of the convex turning at the hub, increases by 34.6%, 84.6%, 192.3% and 430% for the 10%, 20%, 30% and 40% bleed cases, compared to the 0% bleed case. The thick boundary layers for the 30% and 40% bleed fractions indicate that the ICD is separated at this point. That is verified by considering the skin-friction coefficient from Figure 8a) in Paper G. Even though the OGV blades are not included in the simulations in Paper G, the paper provides information on how the end-wall boundary layers behave for different bleed ratios.

4.2.1 OGV separation

The increased incidence and boundary layer thickness, at the hub, has a negative impact on the performance of OGV blades. However, the tangential averaging can hide information about the flow physics, for example, information about localized separation that covers relatively small tangential sections. This is not clearly stated throughout the discussion in the appended papers (Figures 11 and 13 in Paper B, Figure 14 in Paper D, Figure 13 in Paper E, and Figures in 15 and 16 Paper F). Therefore, this section will focus on clarifying some of the main flow physics in the OGV blade row.

Taylor [69] presented an example of different types of compressor separation, that occur in 2D and 3D. Additionally, the separation as a function of incidence was investigated. Hah and Loellbach [30] studied the separation of a compressor stator for two different incidences. A corner-hub separation formed on the suction side of the stator blade, where the location and strength of the vortices depended on the blade loading (incidence in this case). Friedrichs et al. [24] compared two different stator designs at two different operating conditions, at the design point and part load. The main focus of the study was to investigate the stator-hub and blade flow. Taylor and Miller [70] focused on two main flow mechanisms that have a severe impact on the performance of a compressor blade: open corner separation and 3D trailing edge separation. An open corner separation is a 3D mechanism causing the end-wall flow to separate. It is a transient phenomenon, sensitive to the incidence angle.

In the appended papers, the total pressure contours were used to present the flow field downstream of the OGV blades, but even though it presents regions of substantial losses, it is difficult to draw a clear conclusion if the flow is separated. To improve the analysis, Figure 4.3 presents the average axial velocity contours at the OGV_{out} evaluation surface (Paper F: U_{ave} from Eq. 6 and OGV_{out} from Figure 3). The scale in Figure 4.3 extends from zero velocity, where large blue regions represent negative values, and therefore, separated flow structures. The circle markers (●) represent the OGV blades upstream of the struts (OGV^s) and the square markers (■) represent the OGV blades located upstream of the ICD mid-blade-passage (OGV^{mbp}). All operating conditions experience separated flow on the OGV blades that are directly upstream of the struts. For the 0% bleed case, signs of small corner separation is visible at both end-walls for all blades. The corner-casing separation is, however, decreasing with increased bleed fractions as the casing boundary layer is extracted through the bleed pipe, whereas the hub-corner separation increases in magnitude as the bleed increases. For the 40% bleed case, the

separation region increased substantially and resulted in an open hub-corner separation for the blades upstream of the struts and the blades located upstream of the strut's mid-blade-passage.

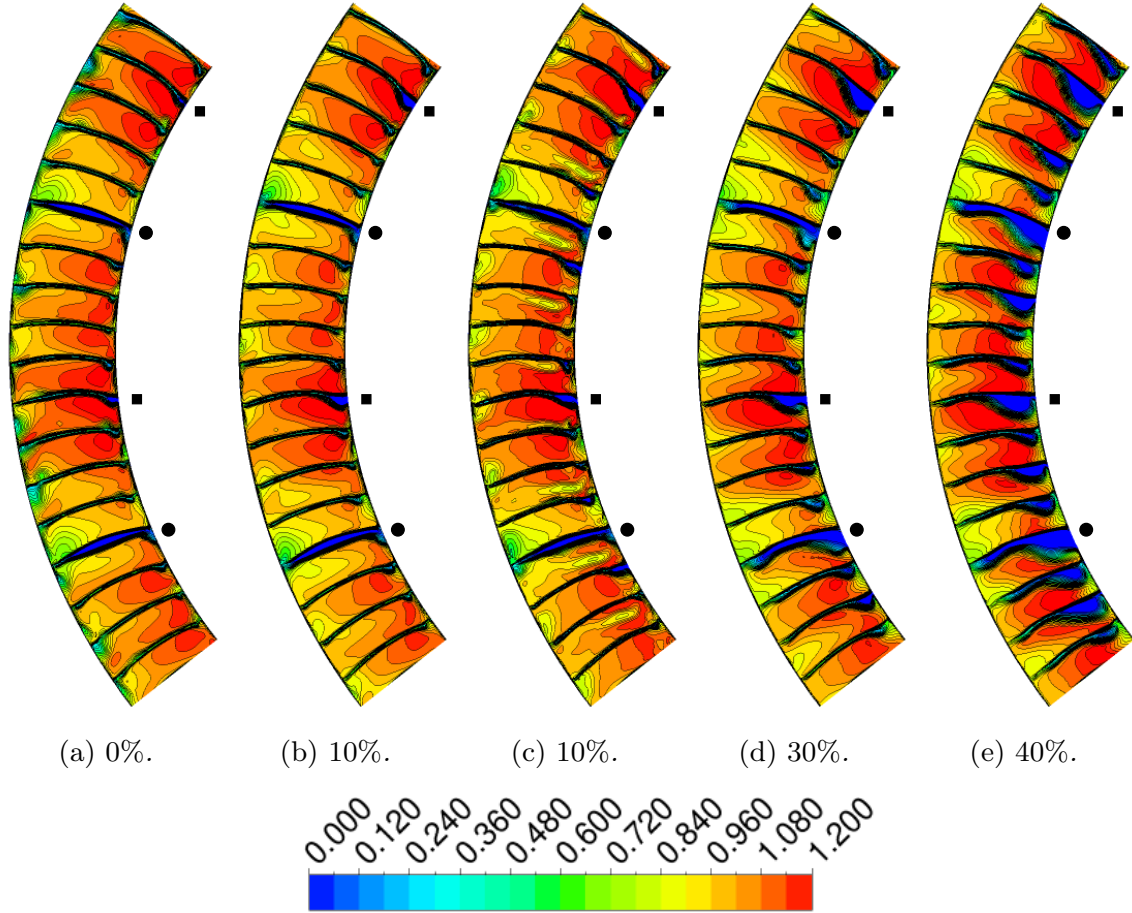


Figure 4.3: *Normalized axial velocity at the OGV_{out} evaluation surface (Paper F). SBES results presented in sub-figure (c).*

To quantify the magnitude of the separation, the streamlines on the suction side of two OGV blades are presented in Figure 4.5. The streamlines are shown for the operating conditions presented in Paper F (SST: 0%, 10%, 30%, 40% and SBES: 10%). The OGV blades presented are upstream of the ICD mid-blade-passage (upper ■ in Figure 4.3: OGV^{mbp}) and upstream of the strut (upper ● in Figure 4.3: OGV^s). The span-wise location of the corner-hub vortex focal point and the axial location of the corner-hub separation is marked in the figures with ● and ●.

In Table 4.2, the location of the focal point center (●) at the OGV^{mbp} and the OGV^s blade suction sides is presented in terms of normalized span. The vortex diffuses further away from the hub with increased bleed fraction. However, for the OGV^s blade and the 30% bleed case, it is difficult to identify a single vortex structure due to complicated secondary flow features, resulting in a similar location as for the SBES-10% case. Additionally, in the 40% case the hub and casing boundary layers have collided and formed a single vortex

Table 4.2: Span-wise location of the corner-hub vortex (\bullet , Figure 4.5).

	SST-0%	SST-10%	SBES-10%	SST-30%	SST-40%
OGV ^{mbp}	14%	17%	25%	31%	43%
OGV ^s	10%	13%	25%	24%	37%

Table 4.3: Corner-hub separation location (\bullet) as a percentage of blade chord length (Figure 4.5).

	SST-0%	SST-10%	SBES-10%	SST-30%	SST-40%
OGV ^{mbp}	60%	58%	52%	24%	15%
OGV ^s	59%	58%	56%	27%	0%

structure located at 43% and 37% span for the OGV^{mbp} and OGV^s blades, respectively.

In a similar way, the axial location of the corner-hub separation (\bullet) at the OGV^{mbp} and the OGV^s blade suction sides is presented in Table 4.3. The suction side is separated for all operating conditions on both blades. As expected, the separation is located close to the trailing edge for the 0% bleed case but moves upstream towards the leading edge with increased amount of bleed. The axial location of the separation is similar for both blades under the same operating conditions, except for the 40% bleed case where for the OGV^s blade corner-hub separation extends to the leading edge.

Comparing the secondary flow structures on the OGV^s and the OGV^{mbp} blades in Figure 4.5, a couple of differences can be identified. The axial location of the separation line at mid-span is closer to the leading edge at the OGV^s blade. This is caused by the strut's potential field, increasing the downstream blockage. The blockage from the strut, in combination with the radial pressure gradient, forces the flow near the casing towards the hub. This is evident for the 30% and 40% bleed ratios, where the streamlines extend from the casing to the hub, before rolling up into the corner-hub vortex. Additionally, the streamlines are presenting to what extent the separation occurs, as seen in Figure 4.3.

4.3 ICD with an integrated strut

As for the OGV and the PSW blades, a more detailed description of the governing flow physics in an integrated S-shaped duct can be provided, in addition to the discussions from the appended papers. The integrated system studied in this thesis has an upstream PSW, a rotor off-take bleed, an LPC's OGV blade row and an integrated strut. Those components will all contribute to the complicated flow behavior and secondary flow structures in the duct. The geometry of an S-shaped duct can be characterized using four parameters (A_{ex}/A_{in} , L/h_{in} , $\Delta R/L$ and $r_{m,in}/r_{m,out}$, Table 1 from Paper G). Additionally, by introducing an integrated strut, the thickness-to-chord ratio (t/c) is added to the characteristic parameters. Integrating a strut into the S-shaped duct introduces a critical point for separation. The risk of separation is highest in the deceleration region at the intersection between the strut and the hub end-wall (Figure 4.4). The increased risk is because the flow is not only diffused due to the S-shaped duct but also due to the

decreasing thickness of the strut towards the trailing edge [45, 36]. Therefore, increasing the thickness-to-chord ratio of the strut will make the duct more prone to separation. The risk of separation is not as high at the casing due to the stream-wise curvature.

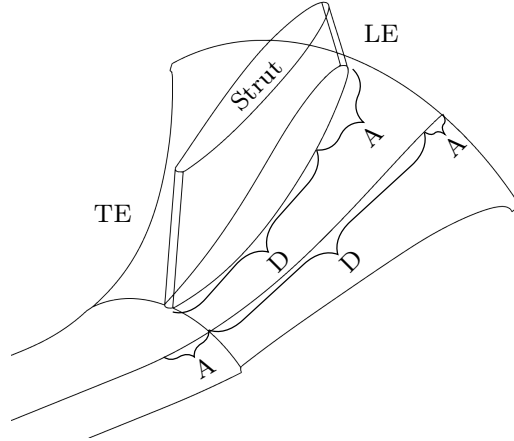


Figure 4.4: Acceleration (A) and deceleration (D) regions on the inner casing of an S-shaped duct with an integrated strut.

Most publications on the performance of S-shaped intermediate compressor ducts have area-ratios equal to unity [45, 47, 66, 75, 74, 76]. A constant area ratio results in a relatively low acceleration of the bulk flow. Even though the area of the duct is constant, the increased blockage due to the strut and a thicker boundary layer results in accelerated flow [10]. The ICD studied in this thesis has, however, a decreasing area ratio ($A_{ex}/A_{in}=0.67$). The decreasing area ratio results in an accelerated bulk flow, decreasing the deceleration due to the stream-wise curvatures and the strut geometry. For the current strut design, the maximum and trailing edge thickness-to-chord ratio at mid-span is $t_{max}/c = 0.17$ and $t_{TE}/c = 0.004$, respectively, *i.e.* a relatively low diffusion is caused by the strut. The struts in the literature usually have a thickness-to-chord ratio between 0.2 and 0.3 [45]

To estimate the performance of the ICD presented in Papers B, D, E, and F, an extension is made to Paper F to identify if, and to what extent, the flow is separated. In Paper F, an 80° tangential sector is simulated (two strut blade passages) for four different bleed ratios using the $k - \omega$ SST turbulence model (0%, 10%, 30% and 40%) and a single bleed ratio using the hybrid SBES hybrid model (10%). Figure 4.6 presents the iso-surfaces of negative axial-velocity, including the OGVs and the struts for the five simulations. For each bleed ratio, detailed views are presented of the trailing edge of the strut, close to the hub (A), and of the OGV^s blade (B). With an increasing bleed ratio, three flow features are affected.

Firstly, the separation region upstream of the OGV blade row, at the bleed pipe splitter, is largest for the 0% bleed case, when no flow is extracted through the bleed pipe. Furthermore, the region is smallest for the 30% bleed, meaning that there is an optimum bleed if the aim is to limit the bleed pipe splitter separation. Secondly, the separation on the OGV^{mbp} and the OGV^s blades increases with an increased bleed ratio. This coincides

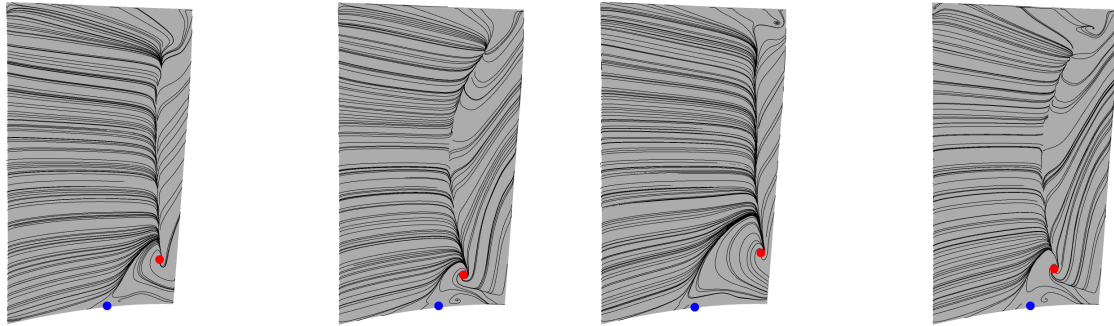
with the behavior observed previously in Figure 4.5 and Tables 4.2 and 4.3. For the 40% bleed ratio, the enlarged figure of the OGV^s blade (B) in Figure 4.6, indicates that the separated region extents to the leading edge of the strut. Additionally, for the 40% bleed case, the OGV^s blade passage is fully blocked near the hub (Figure 4.6 e)-B). Thirdly, when considering the enlarged figure of the strut's trailing (A), the separation region increases with increased bleed. Additionally, the 40% bleed ratio is separated near the leading edge. For all cases, a small separation region was observed along the strut-hub intersection (not visible in Figure 4.6). This is caused by a corner vortex.

The negative axial velocity indicates where the flow is separated and therefore, origins of high losses. However, since the flow is guided through a radial offset, the separation can occur in the radial direction. This separation is not captured by the iso-surfaces presented in Figure 4.6. Therefore, to verify if the flow is separated in ICD, the streamlines on the strut are presented in Figure 4.7 (right hand strut in Figure 4.6). The markers in the figure are placed to locate the leading edge strut-hub streamline at the leading and trailing edges (●), the streamline from the leading edge boundary layer (●) and the separated streamline at the trailing edge (●), both the axial location and the height of the blockage. The exact values are given in Table 4.4. The strut-hub streamlines (●) diffuse towards the casing with increased bleed. However, for the SBES simulation, the strut-hub trailing edge streamline is at 38% higher span compared to the SST-10% case. The leading edge boundary layer streamlines, at the trailing edge (●), are located at a higher span for the 30% and 40% bleed cases. However, the boundary layer thickness at the leading edge is thicker for those two cases and therefore the diffusion is less, compared to the other cases. The axial location of the separation point (●) at the strut-hub interface, moves further upstream along the strut, with increased bleed ratio. This is the same behavior as observed in Figure 4.6. Furthermore, the separation region extends to higher radii with increased amount of bleed. The SBES-10% case shows signs of significantly less trailing edge separation, as visualized in Figure 4.6. Table 4.4 shows that the SBES results are separated at a location closer to the trailing edge and the separation region extends less in the radial direction, compared to the SST result (even the 0% bleed case).

Table 4.4: Locations of critical strut streamlines from Figure 4.7.

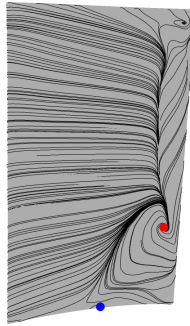
Case	strut-hub (●)		LE boundary layer (●)		TE separation (●)	
	LE (x/c)	TE (x/c)	LE (x/c)	TE (x/c)	span (r/h)	axial (x/c)
SST-0%	0	0.37	0.2	0.61	0.08	0.89
SST-10%	0	0.39	0.2	0.59	0.23	0.89
SBES-10%	0	0.54	0.2	0.57	0.06	0.92
SST-30%	0	0.60	0.32	0.64	0.25	0.84
SST-40%	0	0.64	0.33	0.64	0.38	0.72

Figure 4.9 presents the streamline from the left blade passage shown in Figure 4.6. The view is oriented from underneath the duct in a positive axial direction. The surfaces are shown in the lower right corner, where the axial location of the surfaces are, as a fraction of strut's length, $x/c = -0.04, 0.06, 0.25, 0.44, 0.64, 0.96$ for surface 1, 2, 3, 4, 5 and 6, respectively. The vortex developing on the suction side of the strut is marked with

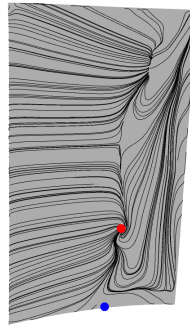


(a) *SST 0%*.

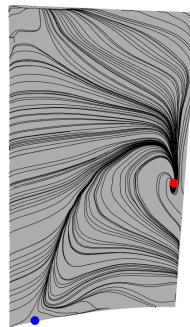
(b) *SST 10%*.



(c) *SBES 10%*.



(d) *SST 30%*.



(e) *SST 40%*.

Figure 4.5: *Surface streamlines on the suction side of the OGV^{mbp} (left) and OGV^s (right).*

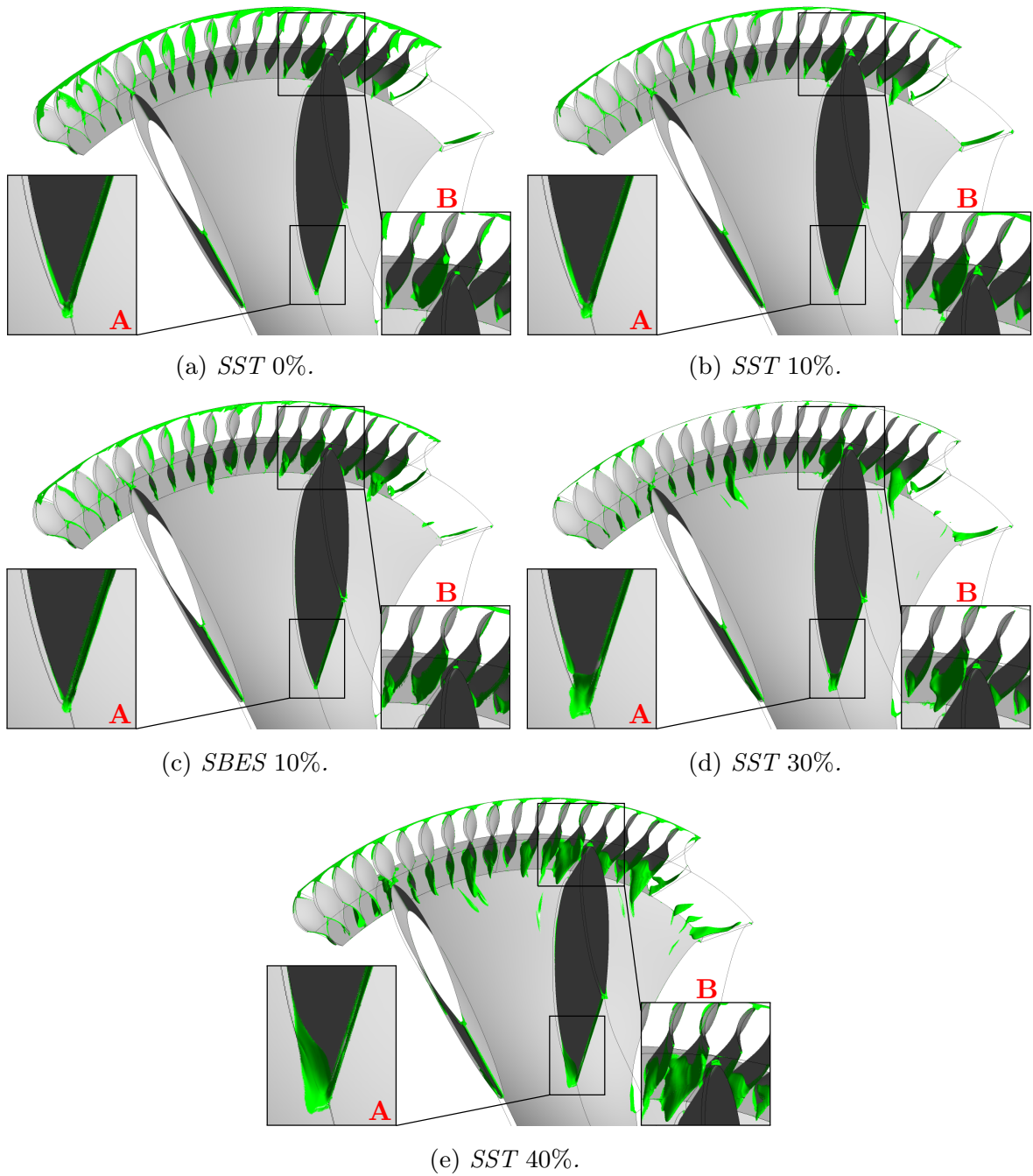


Figure 4.6: *Iso-surfaces of negative axial-velocity with detailed view of the strut's trailing edge and the OGV_s blade.*

letters **A-F**. On Surface 1, the effects of the OGVs are quite prominent. The structures generated from the OGV blades are discussed above. A vortex, close the strut's leading edge, is marked with an **A**. This vortex is formed at the OGV^s blade. The vortex increases in magnitude with increased bleed. The increased magnitude is caused by the increased separation at the OGV blades. The pressure in the passage is increasing from the strut's pressure side to the suction side because of the incidence on the strut's leading edge. Additionally, the pressure increases along the hub, towards the trailing edge of the strut, because of the concave curvature. Combining the two pressure gradients results in a low-pressure region at the suction side of the strut's trailing edge. This low-pressure region is further amplified if the flow is separated at the strut-hub trailing edge. Due to the convex curvature and the OGV separation (if the OGVs are separated), the flow entering the ICD near the hub has relatively low pressure. This low-pressure fluid will follow the path of lowest pressure. Therefore, the hub flow is pushed towards the suction side, magnifying the counter-clockwise rotating vortex (**A**). This behavior results in a large vortex at the trailing edge of the strut. In Figure 4.9, **A-F** mark the development of the vortex.

The same trend is observed for all bleed fractions, where the vortex interacts with the hub-strut boundary layer and the incoming flow from the blade passage. The vortex increases in magnitude and attaches to the strut (due to the pressure gradient). This is the vortex observed at the NRT evaluation surface in papers B, D, E and F. The SBES-10% results, on the other hand, do not show the strong vortex forming on the suction side. Furthermore, the SBES results deliver more uniform flow downstream of the ICD. The losses, seen in Figure 17 in Paper F, are caused by the mixing of the OGV wakes. The OGV blades are separated, resulting in higher losses for the lower half of the annulus at the NRT evaluation surface (Figure 17, Paper F).

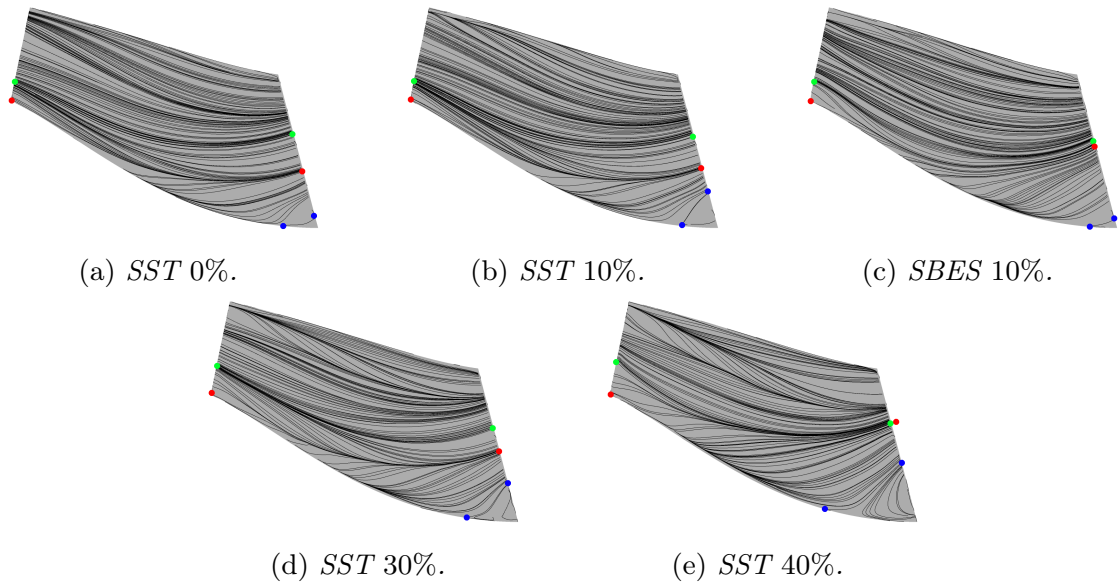


Figure 4.7: *Streamlines on the strut's suction side.*

4.4 Data normalization

As discussed earlier, extracting substantial amount of bleed upstream of the ICD has a severe impact on the performance of the duct. However, to compare different operating conditions, the data has to be appropriately normalized. For papers B, D and E, the dominating normalization was either a pressure ratio or pressure coefficient, where for both parameters, the inlet conditions were used. The reason for using the inlet condition was that it was the only available reference point from the measurements. The dynamic pressure of the traverse measurements was too unstable to be used. Using the inlet conditions can be acceptable if a single operating condition is compared. However, it can give different results if the absolute pressure varies between CFD simulations and/or the experiments.

The problem when defining the reference point at the inlet boundary when comparing different bleed fractions, is that all bleed fractions have same inlet conditions (total and static pressure). However, the flow downstream of the bleed pipe is subjected to new flow conditions (different mass-flow, for example). Using an incorrect reference point can result in misinterpreted flow mechanisms, such as the magnitude of the pressure gradient, as is seen in Figure 4.8. In Figure 4.8 b), the wall-pressure is normalized with the inlet total-pressure and in Figure 4.8 a) the pressure coefficient is used. The pressure coefficient is defined as

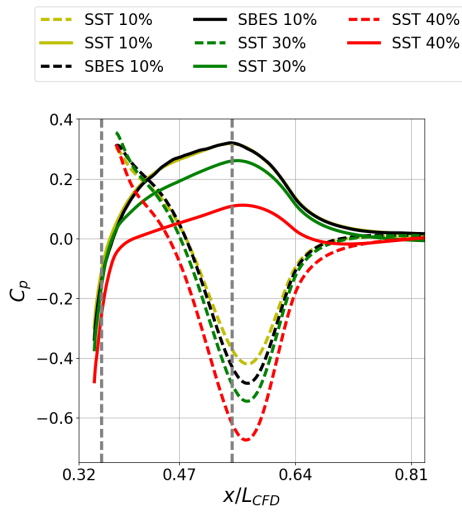
$$C_p = \frac{p - \tilde{p}}{\tilde{P} - \tilde{p}} \quad (4.1)$$

where \tilde{P} and \tilde{p} are mass-flow averaged values of total and static pressure, respectively, over a specific surface (the outlet of the domain for this discussion).

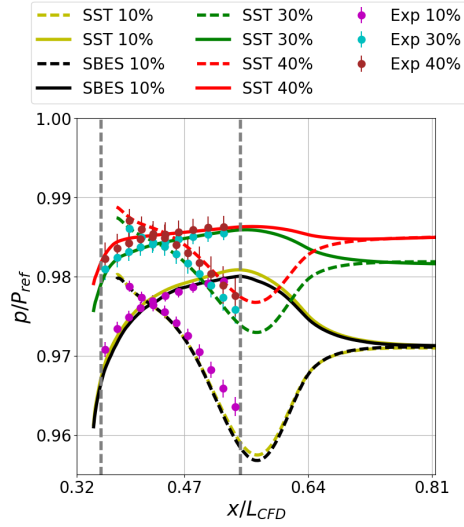
The pressure gradient for the two plots is compared in Table 4.5. Considering the pressure ratio (p/P_{ref}), the 10% bleed case is observed to have the largest pressure gradients, both at hub and casing. However, the pressure gradients for the 40% bleed case are the weakest. When comparing the pressure in terms of pressure coefficient, with the reference point defined at the outlet of the domain to account for the lower mass-flow for higher bleed, more similar pressure gradients are observed for different bleed fractions. The pressure gradients, for the 10% and 40% bleed cases, differ 11% and 15% for the hub and casing, respectively. Furthermore, the pressure gradient at the casing is greatest for the 40% case. This shows the importance of normalizing the data with relative reference points.

Table 4.5: Pressure gradients at the ICD's end-walls.

Mode	10%		30%		40%	
	hub	casing	hub	casing	hub	casing
p/P_{ref}	2%	2%	1.0%	1.4%	0.7%	1.1%
ΔC_p	0.66	0.73	0.63	0.9	0.59	0.98



(a) Static pressure coefficient (C_p), using the outlet as a reference point.



(b) Static pressure normalized with inlet total pressure [53].

Figure 4.8: Wall pressure in the strut's mid-blade-passage. Dashed line: casing and solid line: hub. The vertical gray dashed lines represent the axial location of the leading and trailing edges of the strut.

4.5 Conclusion

This chapter explained the flow physics in an integrated ICD, including an upstream PSW, bleed pipe, OGVs and an integrated strut. The explanation extends the discussion in the appended papers (based on the results from Paper F), with a more detailed description of the secondary flow structures and loss mechanisms.

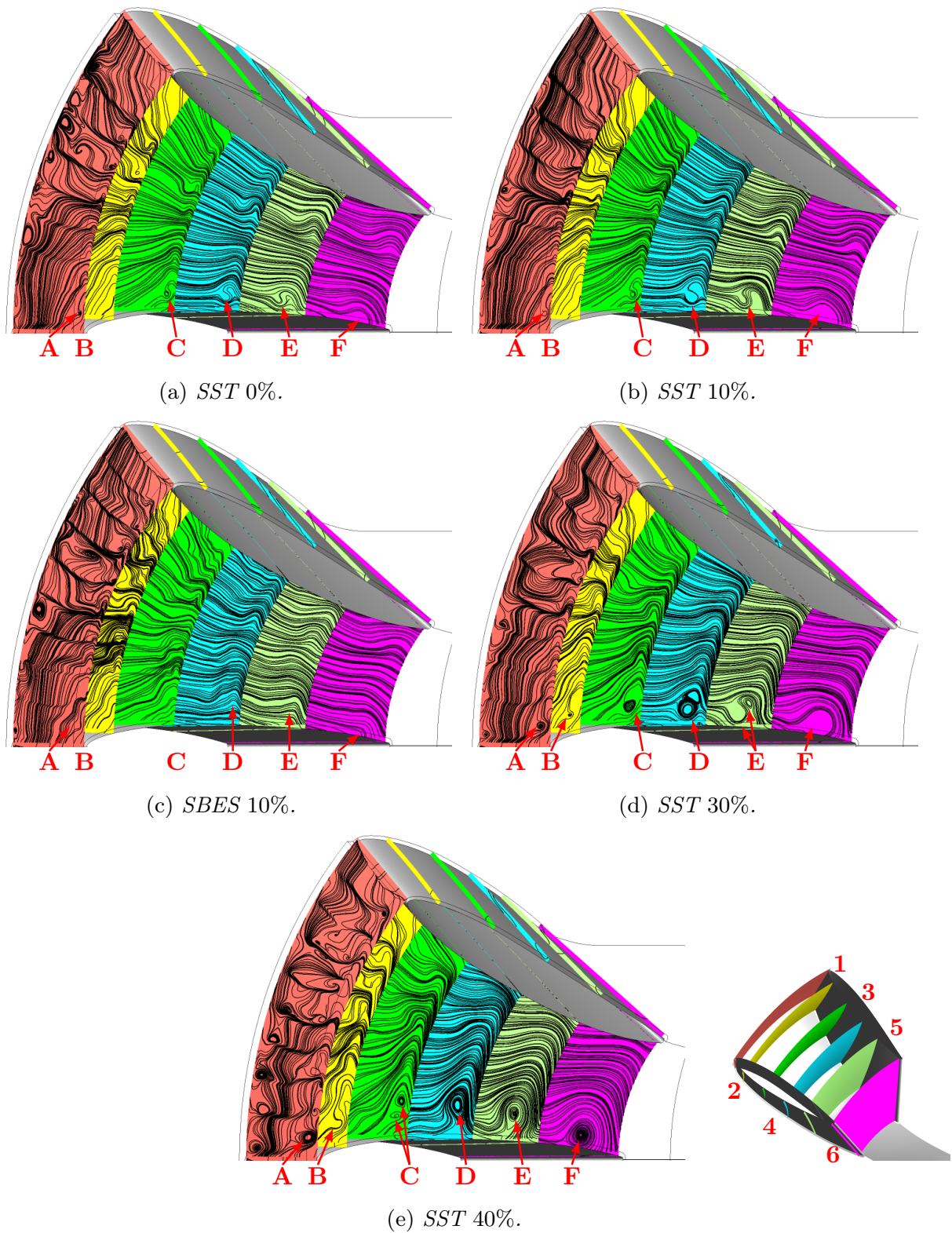


Figure 4.9: Streamlines in the strut's mid-blade-passage (hub removed to visualize the streamlines). The small figure in the lower right corner shows the location of the surfaces 1-6 (the hub visible).

Chapter 5

Summary of papers

5.1 Paper A

E. M. V. Siggeirsson, N. Andersson, and F. Wallin. “Sensitivity study of the SA-DDES shielding function”. *AIAA Scitech 2018 Forum*. Kissimmee, Florida, 2018

Division of work

Besides being the main author, my contribution consisted of grid generation, performing CFD simulations, and post-processing and analyzing the results. Additionally, my contribution was to implement the SA one-equation turbulence model and the DDES model into G3D::Flow. The co-authors supervised the work and provided feedback on the analyzed results. Furthermore, the geometry was provided by GKN Aerospace.

Summary

In this paper, different versions of the DDES model’s shielding function were applied to a single PSW blade to characterize the performance of the model. The original DDES model was found to provide insufficient protection of the boundary layer when the stream-wise cell size was relatively small. Consequently, the model’s sensitivity to various coefficients in the shielding function (which were calibrated by performing a flat plate simulation) was evaluated. Based on this evaluation, the C_1 coefficient was doubled, resulting in better shielding performance. However, the performance of the modified function was not ideal because it extended far beyond the boundary layer on the suction side of the blade. Having the shielding function extending outside the boundary layer is preferred over the opposite, as the grid density in the boundary layer is not sufficient for LES. Therefore, the new version should be used when simulating the PSW blade. When this work was presented, it was pointed out that the insufficient shielding of the original model could be caused by the low inlet turbulence intensity. It was also noted that the inlet boundary condition might necessitate the introduction of synthetic turbulence to maintain a continuous transition from the modeled turbulent stresses inside the RANS region to the resolved stresses in the LES region.

Discussion

This paper showed the necessity in analyzing the performance of the shielding function when using the DDES model, even though the shielding function was initially supposed to handle ambiguous grids. Additionally, it provided important information for future simulations on the ICD geometry using G3D::Flow and DDES. Furthermore, based on the time-step requirements for the transient simulations, the total simulation time for the fully integrated design meant that using G3D::Flow was not practical without any modifications to the code as the simulations would take years.

5.2 Paper B

E. M. V. Siggeirsson, N. Andersson, and F. Wallin. “Numerical and experimental study on bleed impact on intermediate compressor duct performance”. *ASME 2018, Turbo Expo*. Oslo, Norway, 2018

Division of work

As the main author, my contribution consisted of grid generation, performing CFD simulations, post-processing and analyzing the results, both from the CFD simulations and the experiments. Ulf Johansson and Steffen Hammer at GKN Aerospace conducted the experiments and provided support for the post-processing of the experimental data. The co-authors supervised the work and provided feedback on the analyzed results. Furthermore, the geometry was provided by GKN Aerospace.

Summary

This paper presents a comparison between experiments and CFD simulations using G3D::Flow, where the Spalart-Allmaras one-equation turbulence RANS model was used. The geometry represents an ICD from a turbofan engine with an integrated bleed pipe, OGVs and struts. Instead of an upstream rotor, the flow is turned using a PSW blade row. Two different operating conditions were considered, where 10% and 31% of the inlet mass-flow was extracted through the bleed pipe. For the lower bleed fraction case, the simulations agreed well with the experimental data in terms of radially averaged profiles and static wall-pressure. However, there were significant differences observed when comparing the measurements and CFD in terms of contours of total pressure. For the higher bleed fraction case, the simulations exhibited pronounced instability that adversely affected the convergence. This was attributed to the fact that the bleed pipe was relatively short, which meant that the boundary condition at the bleed pipe outlet strongly affected the simulations’ progress. It was, therefore, suggested that the bleed pipe should be extended in future simulations of systems with high bleed fractions.

Discussion

Despite that the simulation for the higher bleed fraction had convergence issues, the lower bleed case showed the solver’s capability of predicting the experimental values in terms of radial profiles and wall-pressure, even though the more common RANS method was used. The contour plots of static pressure showed higher losses for the lower bleed fraction but as discussed in Chapter 4, the averaging method and reference points are important when comparing the flow downstream of the bleed pipe.

Figure 5.1 presenting the same data as shown in Figure 13 and 14 but in terms of the total pressure coefficient (Eq. 4.1) with the reference point at the exit of the domain. By using the exit of the domain, the dynamic pressure of the extracted bleed flow is excluded from the comparison. This shows the importance of comparing the data with a more suitable reference point. When the pressure coefficient is compared, the minimum value

in the strut's wake (point **A** in the figure) for the 10% bleed is -0.38 , whereas for the 31% bleed it decreases to -0.44 . For the secondary vortex on the left (point **B** in the figure), the value decreases from -0.26 to -0.34 . Furthermore, the low-total pressure region is larger for the higher bleed case. This is an opposite behavior observed in the paper, where the higher bleed fraction showed signs of less losses due to the inaccurate normalization.

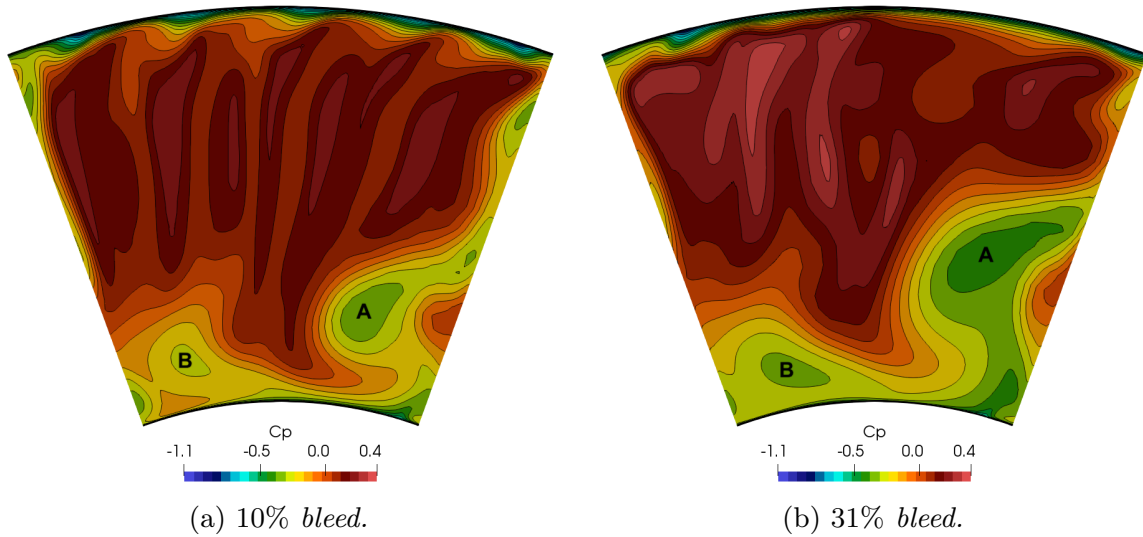


Figure 5.1: Total pressure coefficient (C_P).

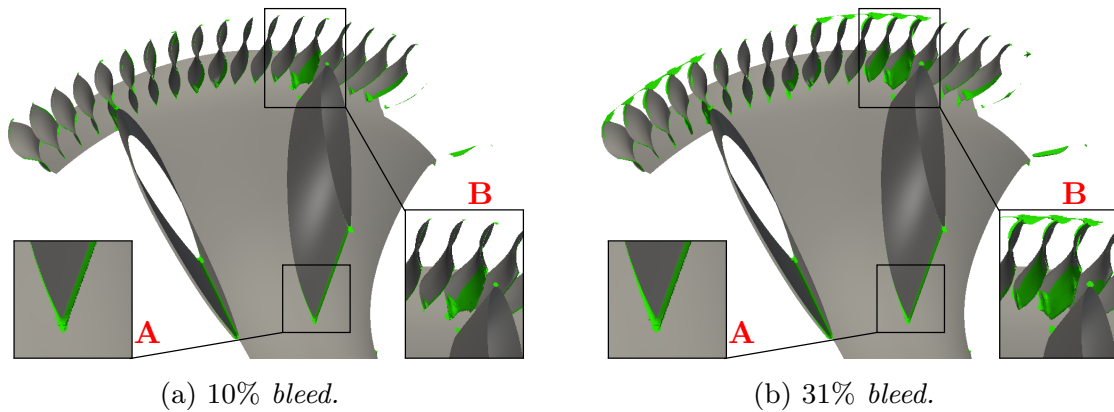


Figure 5.2: Iso-surfaces of negative axial velocity. Only single strut blade-passage simulated. Two blade-passages are presented for better visualization.

In the paper, it was concluded that the risk of separation was higher for lower bleed fraction. This assumption was made from the static wall-pressure distribution on the duct's end-walls (Figure 6 and 7 in the paper). The inlet was used as a reference point to obtain the pressure coefficient and therefore, the different bleed fractions were not compared in relative terms. As seen in Figure 5.2, the separation at the strut's trailing edge (detailed view **A**) and at the OGV blades (especially at the blades upstream of the

strut (detailed view **B**)), increases with increased bleed. Increased bleed ratio increases the swirl and the boundary layer thickness at the OGV inlet, causing an unfavorable incidence on the OGVs resulting in separated flow (Paper F and Chapter 4). Firstly, the separated flow at the OGVs increases the risk of ICD separation due to low quality flow. Secondly, the thicker boundary layer increases the risk of separation at the critical strut-hub intersection [60]. Furthermore, limitations to the experimental data are discussed in Chapter 4.

5.3 Paper C

E. M. V. Siggeirsson and N. Andersson. “The NASA 2D wall-mounted hump simulated using DDES-SA with the G3D::Flow solver”. *AIAA Scitech 2019 Forum*. San Diego, California, 2019

Division of work

Besides being the main author, my contribution consisted of grid generation, performing CFD simulations, and post-processing the results. Furthermore, my contribution consisted of the implementation of the SLA length scale into G3D::Flow and exploring the available acceleration techniques for the dual-time-stepping method. The co-author supervised the work and provided feedback on the analyzed results.

Summary and discussion

A well-documented test case, the 2D NASA wall-mounted hump, was simulated using G3D::Flow. The paper is divided into three objectives: First, the implementation of the SA-turbulence model into G3D::Flow was verified simulating the hump configuration. Additionally, a grid-dependency study was performed to verify the results and the grid-topology. Second, the grid-topology was used for further simulations using the DDES model, where an SLA length scale was used instead of the $\max(\Delta x, \Delta y, \Delta z)$, which is the length scale from the original model. The SLA length scale adjusts the length scale to take the direction of the vorticity into account and, therefore, uses the flow physics to set the limit on the resolvable scales. This is especially beneficial for industrially focused grids, where the spacing in one direction can be substantially larger, compared to the other two directions. Third, the paper explores the application of a dual-time-stepping (DT) time-marching technique for G3D::Flow. The benefit of the DT method is a time-step based on physics instead of numerics. There were two simulations performed using the DDES model and the SLA length scale (DDES1 and DDES2), where a significant difference was observed for the separation and the reattachment points. In Figure 7, the DDES2 simulation attached at the back wall of the hump, then separated, before attaching to the horizontal wall downstream of the hump ($x/C_{s1}^{\text{DDES2}} = 0.665$, $x/C_{a1}^{\text{DDES2}} = 0.715$, $x/C_{s2}^{\text{DDES2}} = 0.902$ and $x/C_{a2}^{\text{DDES2}} = 1.255$). The DDES1 simulation and a RANS simulation, performed on the same grid as the DDES2 simulation, separated at the hump and reattached downstream ($x/C_{s1}^{\text{DDES2}} = 0.665$, $x/C_{a1}^{\text{DDES2}} = 1.14$), $x/C_{s1}^{\text{RANS}} = 0.665$ and $x/C_{a1}^{\text{RANS}} = 1.23$). The two later simulations showed a similar behavior, in terms of number of separation points,

as observed in the measurements ($x/C_{s1}^{\text{EXP}} = 0.665$ and $x/C_{a1}^{\text{EXP}} = 1.1$). It was concluded that the incorrect predictions were caused by insufficient grid resolution in the focus region, behind the hump. However, one of the DDES simulations showed a substantial improvement in the reattachment location. There, the smaller cells caused a faster transition from RANS to LES, resulting in the improved prediction. Additionally, even though the results showed a great acceleration of the time-marching solver, a great effort had to be put in adjusting different parameters. This challenge was the motivation for implementing a 5-stage Runge-Kutta DT method and an alternative implicit residual smoother into G3D::Flow (discussed in Chapter 3).

5.4 Paper D

E. M. V. Siggeirsson, N. Andersson, and M. O. Burak. “Integrated Compressor Duct with Bleed: Experimental Validation of a Hybrid RANS/LES Approach”. *24th ISABE Conference*. Canberra, Australia, 2019

Division of work

Besides being the main author, my contribution consisted of grid generation, performing CFD simulations, and post-processing and analyzing the results. The co-authors supervised the work and provided feedback on the analyzed results. GKN aerospace provided the geometry and experimental data.

Summary

CFD simulations were performed on the same configuration, as discussed in Paper B, where an experimental test rig at GKN Aerospace was simulated. The configuration had an extended bleed pipe to minimize the effects from the bleed pipe boundary condition when extracting a significant amount of the inlet mass-flow through the bleed pipe. A single operating condition was simulated, where 40% of the inlet mass-flow was extracted through the bleed pipe. The simulations were performed using ANSYS CFX. The reason for using ANSYS CFX instead of G3D::Flow was because it is an implicit CFD solver, allowing for time-steps based on physics instead of numerical stability. Furthermore, the application of a hybrid RANS/LES turbulence model was analyzed, where the hybrid model, Stress Blended Eddy Simulation (SBES) model, was used and compared to experimental data and a common RANS turbulence model. As discussed in the extended summary, the SBES model has been proven successful in protecting the boundary layers. The boundary layers were modeled using an automatic wall-function, except for a single RANS simulation for comparison. Comparing the two CFD methods, the SBES model resulted in an improved prediction of the experimental data, especially when comparing the total pressure profiles downstream of the ICD. The wall-resolved RANS simulation over-predicted the separation at the OGV blades, resulting in a substantial increase in losses. The hybrid model provides realistic, transient behavior, whereas the time-averaged RANS result will never exist in reality. This difference was emphasized by considering how significantly different the flow field delivered to the downstream HPC could be. The

instantaneous ICD’s exit swirl, deviated -18° to 17° from the time-averaged swirl, for the hybrid method. Additionally, the different CFD methods were compared in terms of computational cost. As expected, the hybrid simulations were significantly more expensive, compared to the RANS simulations.

Discussion

The paper provided results from hybrid simulations in a reasonable time-frame. The paper showed the benefit of performing hybrid simulations in terms of transient flow behavior. Furthermore, the hybrid model showed improved predictions of the experimental data. However, the discussion regarding the flow mechanism in an S-shaped duct could be improved. In the paper, the critical location for separation was defined as the second, concave bend at the hub. Although this is true, the critical point can be located at the peak of local diffusion, near the trailing edge of the strut, at the strut-hub intersection.

Additionally, secondary flow structures can be explained in more detail. The vortices, observed at the FT evaluation surface (Figure 8 and Figure 12), were identified as horseshoe vortices generated at the PSW’s leading edges (Chapter 4). All simulations capture the behavior of the horseshoe vortex. However, for the WR-SST-Coarse simulation, the vortex is occupying a sufficient tangential sector and with higher losses to affect the circumferential averaged value. The higher losses result in a 0.1% difference in the radial profile of averaged total pressure at 80% span.

In Figure 11, the wall pressure in the middle of the strut’s blade passage is presented, normalized with the inlet conditions (this is acceptable as only one operating condition is considered). Even though all CFD simulations are capable in reproducing the measurements, the WR-SST-Coarse results predicts a 34% larger pressure gradient from $x/L_{CFD} = 0.36$ – $x/L_{CFD} = 0.41$. The larger pressure gradient is probably caused by the increased separation at the OGVs when using a low-Reynolds number model.

Supported by the discussion in Chapter 4, the high losses downstream of the OGVs are caused by corner-hub separation where the OGV blades in the WR-SST-Coarse simulation are completely separated. The mass-flow in the lower 40% span, downstream of the OGVs, as a fraction of the total mass-flow, is 36% for the WF-SST-Coarse and 28% for the WR-SST-Coarse results, indicating a large amount of blockage caused by the separated regions.

The pressure ratio at the NRT evaluation surface was presented in Figure 15. There, the different predictions of the strut’s wake were only presented qualitatively. Additionally, for the different simulations, the center of the wake is located at 45%, 33%, 25% and 25% span and 27%, 31%, 28% and 35% of the tangential sector, for WF-SBES-Fine, WF-SBES-Coarse, WF-SST-Coarse and WR-SST-Coarse, respectively. The difference in the wake’s location shows signs of a strong passage pressure gradient, where the OGV wakes are dragged towards the strut’s suction side.

5.5 Paper E

E. M. V. Siggeirsson, N. Andersson, and M. O. Burak. “Off design simulations of an S-shaped intermediate compressor duct: Experimental validation of DDES and RANS

using G3D::Flow". *AIAA Scitech 2020 Forum*. 2020

Division of work

Besides being the main author, my contribution consisted of grid generation, performing CFD simulations, and post-processing and analyzing the results. The co-authors supervised the work and provided feedback on the analyzed results. GKN aerospace provided the geometry and experimental data.

Summary

The same configuration as in Paper D was simulated with G3D::Flow using two different turbulence models. The simulations were performed using a hybrid RANS/LES model (DDES) and a (U)RANS model (SA). To allow larger time-steps and, therefore, to save computational resources, the boundary layers were modeled using wall-functions ((U)RANS regions). Overall, the CFD simulations were capable of reproducing the experimental data in terms of wall-pressure and upstream and downstream radial total pressure profiles. However, the DDES simulations failed to predict the wall-pressure at the hub in the strut's mid-blade-passage. It was concluded to be caused by the explicit use of wall-functions but as discussed later, this is caused by the different flow predictions upstream of the OGVs. However, for complicated geometries, with complex flow physics, automatic wall-functions should be preferred over explicit.

Discussion

Most of the same discussion as for Paper D holds for this paper in terms of identifying governing flow mechanisms such as the PSW horseshoe vortex at the FT evaluation surface (Figure 12), separation on the suction side of the OGV blades (high losses in Figure 13), the critical point at the strut-hub peak diffusion location and the dependency on how the results are normalized. In the following section, the discussion will be extended to clarify the results of this paper.

In Figure 10, the end-wall pressure at the strut's mid-blade-passage was presented. Neither of the two DDES simulations were able to predict the averaged values from the measurements. The under-predicted pressure is caused by increased separation at the OGV blades, for both DDES simulations. The increased separation causes increased blockage close to the hub, decreasing the mass-flow in the lower half of the domain. The mass-flow in the first 40% span (normalized with the mass-flow through the whole span) was 34% for the URANS results, whereas it was 29% for the DDES-Fine-WF. However, large deviations were observed in the measurements caused by difficulties in achieving the correct operating conditions. This would need further investigations but might be caused by large separation regions at the OGV blades. Taylor and Miller [70] pointed out that an open corner separation is sensitive to the incidence, where small changes in incidence can cause a significant increase in separation and, therefore, losses. This might explain the under-predicted pressure in the DDES simulations. Furthermore, the DDES simulations used 43% bleed, compared to 38% for the (U)RANS simulations, causing

increased swirl upstream of the OGVs. In Figures 5.3 and 5.4, the difference between the URANS-WF and DDES-Fine-WF is presented. Figure 5.3 a) presents the total pressure coefficient upstream of the bleed and shows the same behavior as seen in the contours from Figure 12. The horseshoe vortex generated at the PSW blades is more visible and introduces higher losses near the hub for the DDES-Fine-WF result. The increased losses affect the velocity profile shown in Figure 5.3 b). The boundary layer is two times thicker in the DDES-Fine-WF simulation. The swirl, however, differs insignificantly in the hub boundary layer ($<1\%$). The thicker boundary layer has a significant effect on the downstream locations, where the velocity upstream of the OGV blades is shown in Figure 5.4 a). The boundary layer thickness near the hub increases by 63% and the swirl increases by 5% (Figure 5.4). The swirl increases due to the increased bleed rate. As discussed in Chapter 4, a small changes in hub boundary layer thickness and swirl can increase the separation at the OGV blades significantly, explaining the different results for the DDES simulations.

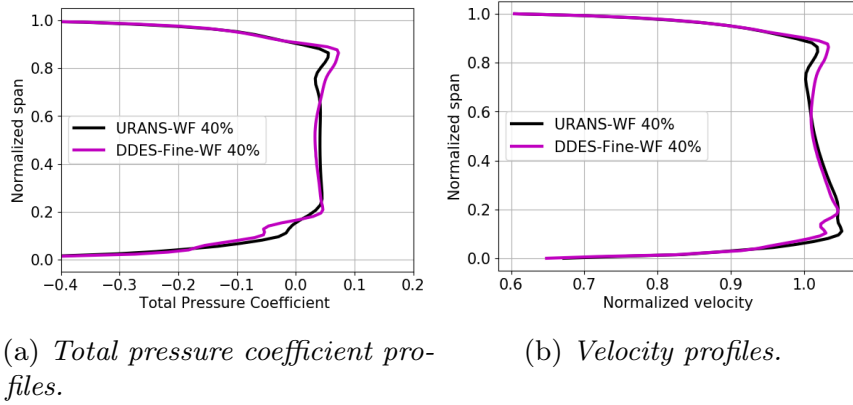


Figure 5.3: Mass-flow averaged radial profiles upstream of bleed.

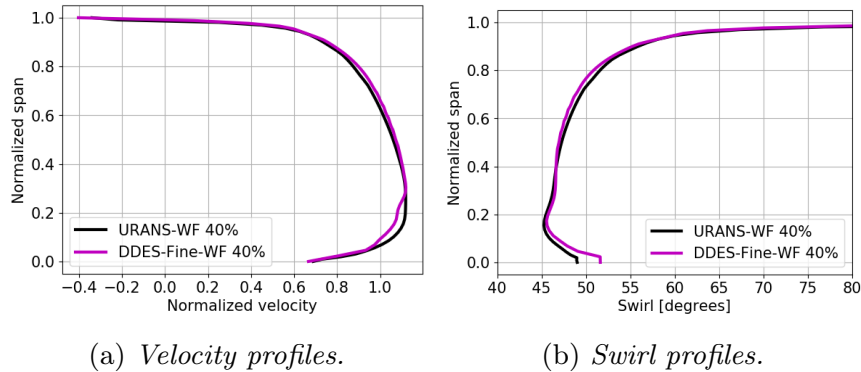


Figure 5.4: Mass-flow averaged radial profiles upstream of OGV.

The reason for different strut's wake for different simulations, in Figure 14, was misinterpreted. The different wakes are caused by secondary flow structures, where the OGV wakes are interacting with the strut's boundary layer. Figure 5.5 shows the

streamlines in the strut's blade passage, on the suction side, and contours of positive radial velocity (the physics are discussed in Chapter 4). Only half of the blade passage is shown and the RANS-WF and DDES-Coarse-WF results are excluded as they yield similar results as the URANS-WF and DDES-Fine-WF, respectively. Figure 5.5 shows that the DDES-Fine-WF solution is separated upstream of the first plane ($x/c = 0.20$), whereas the URANS-WF solution shows the same behavior between the second and third plane (at $x/c = 0.43$). The two mechanisms are, however, generated by different physics. The separation for the URANS-WF results is caused by the interaction between the strut's boundary layer and the incoming OGV wakes. This interaction generates a clockwise rotating vortex (a passage vortex) that is observed downstream of the duct, as the large vortex near the hub (Figure 11 b)). The separation for the DDES-Fine-WF is, however, caused by a combination of the adverse pressure gradient, the relatively thick hub boundary layer and over-predicted separation at the OGV blades. The separated flow results in a clockwise rotating vortex. A passage vortex, generated in the same way as for the URANS-WF results, is visible on the third plane. The passage vortex pushes the original vortex up, causing the larger low-velocity region seen in Figure 14. The passage vortex is located at 20% and 26% span at the fourth plane for URANS-WF and DDES-Fine-WF, respectively. This difference is seen in Figure 11, where the passage vortex is located at 14% and 20% span for URANS-WF and DDES-Fine-WF, respectively. The smaller vortex is responsible for the difference in streamlines, observed in Figure 15. There, the streamlines for the DDES simulations, that have relatively large radial gradients extend to 90% of the span (compared to 60% for the URANS-WF results).

It was stated, during the discussion for Figure 15, that the DDES results were significantly more unstable compared to the (U)RANS results. This effect was, however, never quantified. The area-averaged magnitude of the velocity gradients was 36% larger for the DDES-Fine-WF results, even though the time-averaged solution was used. The larger magnitude shows that the DDES-Fine-WF simulation is predicting more structures of different time-averaged velocity.

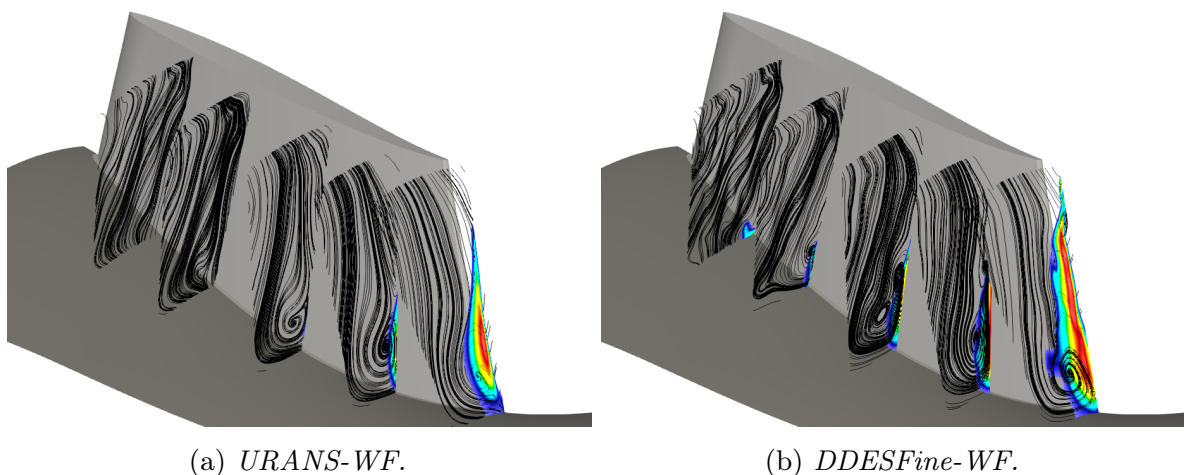


Figure 5.5: *Streamlines on the strut's suction side.*

5.6 Paper F

E. M. V. Siggeirsson, N. Andersson, and M. O. Burak. Numerical and Experimental Aerodynamic Investigation of an S-shaped Intermediate Compressor Duct with Bleed. *Accepted for publication in Journal of Turbomachinery* (2020)

Division of work

Besides being the main author, my contribution consisted of grid generation, performing CFD simulations, and post-processing and analyzing the results. The co-authors supervised the work and provided feedback on the analyzed results. Furthermore, the geometry and experimental data were provided by GKN Aerospace.

Summary and discussion

CFD simulations were performed on a similar ICD configuration as discussed in Paper B, Paper D and Paper E. However, for this paper, the full bleed system was included, instead of a simplified duct. The common denominator for the number of outlet bleed ducts (4) and the number of struts (9) requires the simulations of the whole annulus. Therefore, a simplification was made where a single outlet bleed duct was assumed for an 80° tangential sector to limit the computational requirements of the simulations. Simulations were performed for several operating conditions, where 0%, 10%, 30% and 40% of the inlet mass-flow was extracted through the bleed system. The simulations were performed using ANSYS CFX, where the turbulence was modeled using the $k-\omega$ SST turbulence model for all operating conditions and the SBES model for the 10% case. First, the CFD results were validated with the same experimental data as presented in Paper B, Paper D and Paper E. As for Paper D, the SBES model improved the predictions downstream of the ICD, with an insignificant difference when considering the wall pressure data. Furthermore, the CFD simulations were compared, where effects from different bleed rates were analyzed. The extraction of axial momentum and conservation of tangential momentum caused the velocity swirl upstream of the OGV to increase with increased bleed. The increased swirl caused an unfavorable incidence on the OGV blades. As a result, the ICD's exit profiles are highly dependent on the operating condition. The comparison between the RANS and SBES results show how the later is capable of representing increased details in the flow, where the mixing of the free-stream is significantly greater. The upstream potential effect from the full bleed system was analyzed, where substantial circumferential variations were observed. An extension to the analysis performed in this paper is given in Chapter 4. There, a more detailed description of secondary flow structures and loss mechanism is given.

5.7 Paper G

E. M. V. Siggeirsson, N. Andersson, and M. Lejon. Integrated compressor duct aerodynamics with an integrated rotor off-take bleed. *Submitted to an AIAA Journal* ()

Division of work

Besides being the main author, my contribution consisted of the geometry design, grid generation, performing CFD simulations, and post-processing and analyzing the results. The co-authors supervised the work and provided feedback on the analyzed results.

Summary and discussion

In this paper, the effects on an upstream bleed pipe on the stability of an ICD were studied. No blades were included in the simulations to isolate the interaction between the ICD and the bleed pipe. Furthermore, the inlet boundary condition was specified with pure axial velocity, excluding the changes in swirl due to the extraction of bleed air. Additionally, the paper includes a detailed description of the flow physics in a "clean" ICD and the necessity of the bleed air was discussed. Extracting flow from the main flow path, upstream of the ICD, caused the flow to diffuse from the hub, resulting in a thicker inlet boundary layer, increasing the risk of separation. However, extracting the low-momentum outer casing boundary layer, decreased the losses in the main flow path.

Chapter 6

Concluding Remarks

As discussed in Chapter 1, the aim of this thesis can be divided into two objectives:

1. **Achieve deeper understanding of the flow physics in an ICD with an integrated bleed system and the last stage of the upstream LPC.**

In this thesis, detailed analysis of an ICD with a bleed system integrated into the upstream casing were performed. The main geometry used in this work was from an experimental test rig located at GKN Aerospace in Trollhättan, Sweden. The test section of the rig represents a real component from a modern turbofan engine. However, a PSW is used instead of a rotor from the last stage of an upstream compressor. The PSW was used to lower the complexity when operating the test rig and to simplify the CFD simulations.

Series of CFD simulations were performed on the geometry representing the test section of the experimental rig (Paper B, Paper D, Paper E and Paper F). The risk of separation was expected to increase with an increased bleed rate. For the operating conditions simulated, the flow was separated when a fraction of the inlet mass-flow was extracted upstream of the ICD. The separation was observed for the upstream OGVs and at the critical point of diffusion near the strut's trailing edge, at the strut-hub intersection.

The full-bleed system was included in Paper F. Four different bleed ratios were simulated and the effect on the performance of the integrated system analyzed. Due to the conservation of tangential momentum, the swirling velocity upstream of the OGVs increased with an increased bleed rate. The increased upstream swirl was caused by the extraction of axial momentum through the bleed system. Additionally, the flow was diffused away from the hub, to account for the decreased mass-flow in the upper half of the span. As a result, the OGV's incidence was adversely affected by increasing bleed, resulting in severe separation for the higher bleed fractions. This behavior can have drastic effects on the performance of the engine, from a significant decrease in engine efficiency to complete system failure. Furthermore, significant circumferential variations were observed in the static pressure field upstream of the bleed, showing the importance of including the whole bleed system for accurate predictions.

To isolate the effects an upstream bleed system has on the ICD, a simple configuration with a bleed pipe and no blades was analyzed in Paper G. The pure axial flow was specified at the inlet, resulting in no change in the velocity direction due to the extraction of axial momentum. However, the velocity profiles were drastically affected due to the curvature effects and an adverse pressure gradient, located at the inner casing of the ICD. Additionally, because a substantial amount of flow was extracted through the bleed pipe, the radial velocity near the inner casing increased, increasing the boundary layer thickness. The increased boundary layer thickness made the flow more prone to separation and resulted in major separation for the highest bleed rate.

Paper D and Paper F showed the benefit from using hybrid RANS/LES models. In both papers the ANSYS SBES model was used. Compared to the RANS model, the hybrid model were capable of improving the CFD predictions downstream of the ICD in

terms of circumferentially averaged radial profiles. The DDES simulations in Paper E, were more ambiguous, over-predicting the separation at the OGV blades. This was caused by thick boundary layers and increased swirl upstream of the OGV blades. The measurements for the 40% bleed case show signs of large instabilities, and therefore, it is difficult to make a definite conclusion. In Papers D and F, the hybrid simulations showed that the common RANS models are not capable of reproducing the experimental data to the same extent as the hybrid methods. However, the resolution in the measurements was limited, and therefore, it was difficult to compare the different CFD modeling techniques to the experimental data in terms of localized flow physics. The hybrid models required significantly more computational resources. However, the results from the hybrid models represent the instantaneous flow physics, whereas the RANS solution will never achieve the same level of detail. The increased level of detail can give valuable information, such as the quality of the flow delivered to the downstream component. Furthermore, the computational cost of the hybrid models means that they will not be used for optimization in the near future, resulting in the necessity for using the RANS models.

2. Method development.

It is a continuous process to develop and maintain a CFD solver. To make G3D::Flow capable of performing industrially focused studies, with the current ICD configuration and higher fidelity simulations in mind, several implementations were required. A one equation turbulence model, developed by Spalart and Allmaras (SA), was implemented and verified [58]. Additionally, the Delayed Detached Eddy Simulation model was implemented where the SA model was used as a base RANS model. G3D::Flow is an explicit solver and as a result, time-steps for transient simulations are limited by numerical stability instead of physics. Due to this limitation, the simulation time of the ICD configuration would take 1-2 years with low-Reynolds number models. This was the motivation for the simulations performed in Paper D and Paper E using wall-functions where the simulation time was decreased by two orders of magnitude. To overcome the significant time constrain, a dual-time-stepping method was implemented and verified, where the simulation time is decreased substantially. The decreased simulation time results in a more capable CFD solver for industrially focused studies, especially for transient analysis.

6.1 Future Work

Using PSWs instead of the LPC's rotor has a significant influence on the flow behavior. The PSWs generate stationary wakes, which will impinge on the downstream OGVs at the same location for the whole simulation time. This setup will limit the transient interaction to a large extent, where features like rotating wakes and tip clearance are not included. Therefore, to improve the understanding of the transient nature in the integrated system, the last stage of the LPC should be included (this work is already in progress but is not available to be attached to this thesis).

The integrated geometry that is considered in this thesis represents a rotor off-take (the reasons for using a rotor off-take are discussed in Chapter 1). As discussed earlier, the conservation of tangential momentum, when extracting flow through the rotor off-take,

compromises the stability of the OGV blades and thus the stability of the ICD. An alternative to the rotor off-take is a stator off-take, where the bleed air is extracted downstream of the OGVs, in front of the struts. As the OGV blades are designed to deliver axial flow, the tangential velocity at the OGV's exit is low, resulting in minimized tangential velocity entering the ICD. Low swirling flow entering the ICD is highly beneficial as it is common to design the ICD strut for a relatively low incidence. However, when using a rotor off-take, the OGV blades help reestablish the flow field and lower the radial diffusion of the flow, increasing the stability of the ICD for a wider range of bleed ratios. The difference between the rotor and stator off-takes should be studied for a definite conclusion.

References

- [1] Pat. US 2007/0137175 A1. 2007. URL: <https://patentimages.storage.googleapis.com/f2/fa/58/2b4d6ab1b095c2/US20070137175A1.pdf>.
- [2] Pat. US 7624581B2. 2009. URL: <https://patentimages.storage.googleapis.com/77/fa/49/92a7a71440054d/US7624581.pdf>.
- [3] F. A. Administration. *AIA PC 338-1 Project: INVESTIGATION OF ENGINE POWER LOSS AND INSTABILITY IN INCLEMENT WEATHER*. U.S. Department of Transportation. 2020. URL: https://lessonslearned.faa.gov/11_main.cfm?TabID=1&LLID=49&LLTypeID=2#null.
- [4] Airbus. *Airbus GMF 2016-2035, Mapping Demand*. France: Art & Caractère, 2016.
- [5] F. Amizadeh et al. Analysis of the recent evolution of commercial air traffic CO₂ emissions and fleet utilization in the six largest national markets of the European Union. *Journal of Air Transport Management* **55** (2016), 9–19. DOI: 10.1016/j.jairtraman.2016.04.006.
- [6] N. Andersson, L.-E. Eriksson, and L. Davidson. Large-Eddy Simulation of Subsonic Turbulent Jets and Their Radiated Sound. *AIAA Journal* **43.9** (2005), 1899–1912.
- [7] *ANSYS CFX Theory Guide*. Release 19.1. ANSYS Inc. Canonsburg, Pennsylvania, United States, 2020.
- [8] A. Arnone, M. Liou, and L. Povinelli. Integration of Navier-Stokes equations using dual time stepping and a multigrid method. *AIAA Journal* **33** (May 1995), 985–990. DOI: 10.2514/3.12518.
- [9] N. Ashton, A. West, and F. Mendonça. Flow Dynamics Past a 30P30N Three-Element Airfoil Using Improved Delayed Detached-Eddy Simulation. *AIAA Journal* **54.11** (2016), 3657–3667. DOI: doi:10.2514/1.J054521.
- [10] D. W. Bailey et al. Performance Assessment of an Annular S-Shaped duct. *ASME. Journal of Turbomachinery* **119.1** (1997), 149–156. DOI: 10.1115/1.2841003.
- [11] J. Blazek. *Computational fluid dynamics: Principles and Applications*. Elsevier Science, 2015.
- [12] P. Bradshaw. *Effects of Streamline Curvature on Turbulent Flow*. Ed. by A.D.YOUNG. Technical Editing and Reproduction Ltd, 1973.
- [13] K. Britchford et al. Measurement and prediction of loss in annular S-shaped ducts. *Experimental Thermal and Fluid Science* **9.2** (1994), 197–205. DOI: 10.1016/0894-1777(94)90112-0.
- [14] K. M. Britchford et al. The development of the mean flow and turbulence structure in an annular S-shaped duct. *ASME. Turbo Expo: Power for Land, Sea, and Air* **1.1: Turbomachinery** ():V001T01A144 (1994), V001T01A144. DOI: 10.1115/94-GT-457.
- [15] *The Effect of Operating Conditions on the Aerodynamic Performance of an Integrated OGV and S-Shaped Duct*. Vol. Volume 1: Aircraft Engine; Marine; Turbomachinery; Microturbines and Small Turbomachinery. Turbo Expo: Power for Land, Sea, and Air. V001T03A043. June 2001. DOI: 10.1115/2001-GT-0347. eprint: <https://asmedigitalcollection.asme.org/GT/proceedings-pdf/GT2001/78507/V001T03A043/2414722/v001t03a043-2001-gt-0347.pdf>. URL: <https://doi.org/10.1115/2001-GT-0347>.

- [16] S. Chen et al. Numerical Study of the Air Bleeding Caused Non-Uniformity in Axial Compressor. *Journal of Thermal Science* **29.1** (2020), 219–231.
- [17] A. J. Chorin. *Vorticity and Turbulence*. New York, NY: Springer New York, 1994. DOI: 10.1007/978-1-4419-8728-0_4.
- [18] L. Davidson. *Fluid mechanics, turbulent flow and turbulence modeling*. Chalmers University of Technology. 2018. URL: http://www.tfd.chalmers.se/~lada/postscript_files/solids-and-fluids_turbulent-flow_turbulence-modelling.pdf.
- [19] L. Davidson and S.-H. Peng. “Embedded LES Using PANS”. *6th AIAA Theoretical Fluid Mechanics Conference, Fluid Dynamics and Co-located Conferences*. 2011. DOI: 10.2514/6.2011-3108.
- [20] J. Donghai et al. Optimization of endwall contouring in axial compressor S-shaped ducts. *Chinese Journal of Aeronautics* **28.4** (2015), 1076–1086. DOI: 10.1016/j.cja.2015.06.011.
- [21] L. Erikson. A preconditioned Navier-Stokes for low Mach number flows. *Computational fluid dynamics* **199**, John Wiley, Chichester (1996) (1996).
- [22] L.-E. Eriksson. *Development and Validation of Highly Modular Flow Solver Versions in G2DFLOW and G3DFLOW*. Tech. rep. 9970-1162. Volvo Aero Corporation. Volvo Aero Corporation, 1995.
- [23] A. Favre. “Problems of Hydrodynamics and Continuum Mechanics”. Philadelphia: Society for Industrial and Applied Mathematics, 1969. Chap. Statistical equations of turbulent gases, pp. 231–266.
- [24] J. Friedrichs et al. Effect of stator design on stator boundary layer flow in a highly loaded single-stage axial-flow low-speed compressor. *Journal of Turbomachinery* **123.3** (2001), 483–489. ISSN: 0889504X. DOI: 10.1115/1.1370168.
- [25] T. Ghisu et al. An Integrated System for the Aerodynamic Design of Compressor Systems - Part I: Development. *ASME. Journal of Turbomachinery* **133.1** (2010), 011011–011011–10. DOI: 10.1115/1.4000534.
- [26] T. Ghisu et al. An Integrated System for the Aerodynamic Design of Compressor Systems - Part II: Application. *ASME. Journal of Turbomachinery* **133.1** (2010), 011012–011012–8. DOI: 10.1115/1.4000535.
- [27] S. Grimshaw, G. Pullan, and T. Hynes. Modeling nonuniform bleed in axial compressors. *Journal of Turbomachinery* **138.9** (2016).
- [28] S. Grimshaw, G. Pullan, and T Walker. Bleed-induced distortion in axial compressors. *Journal of Turbomachinery* **137.10** (2015).
- [29] S. Grimshaw et al. “Loss in Axial Compressor Bleed Systems”. *ASME Turbo Expo 2019: Turbomachinery Technical Conference and Exposition*. American Society of Mechanical Engineers Digital Collection.
- [30] C. Hah and J. Loellbach. Development of hub corner stall and its influence on the performance of axial compressor blade rows. *Proceedings of the ASME Turbo Expo* **1.97** (1997). DOI: 10.1115/97-GT-042.
- [31] <http://pw.utc.com>. Accessed: 2018-02-26.
- [32] JADC. *Worldwide Market Forecast 2016-2035*. Tech. rep. YGR-5089. Tokyo, Japan: Japan Aircraft Development Corporation (JADC), 2016.

- [33] A. Jameson and T. Baker. “Solution of the Euler equations for complex configurations”. *6th Computational Fluid Dynamics Conference Danvers, Danvers, MA, U.S.A.*. 1983.
- [34] A. Jameson. “Time dependent calculations using multigrid, with applications to unsteady flows past airfoils and wings”. *AIAA 10th Computational Fluid Dynamics Conference*. AIAA. 1991. DOI: 10.2514/6.1991-1596.
- [35] D. C. Jesperens, T. H. Pulliam, and M. L. Childs. *OVERFLOW: Turbulence modeling Resource: Validation Results*. Tech. rep. NAS-2016-01. Moffett Field, CA, USA: NASA Ames Research Center, 2016.
- [36] M. K. Karakasis et al. “The effect of an upstream compressor on a non-axisymmetric S-DUCT”. *Proceedings of the ASME Turbo Expo*. Vol. 7. GT2010-23404. 2010, pp. 477–486. DOI: 10.1115/GT2010-23404.
- [37] L. Langston. Secondary Flows in Axial Turbines-A Review. *Annals of the New York Academy of Sciences* **934**.1 (2006), 11–26. ISSN: 1749-6632. DOI: 10.1111/j.1749-6632.2001.tb05839.x.
- [38] B. Leishman, N. Cumpsty, and J. Denton. Effects of inlet ramp surfaces on the aerodynamic behavior of bleed hole and bleed slot off-take configurations (2007).
- [39] H. Lu, X. Zheng, and Q. Li. A combinatorial optimization design method applied to S-shaped compressor transition duct design. *Journal of Aerospace Engineering* **228**.10 (2014), 1749–1758. DOI: 10.1177/0954410014531922.
- [40] H. Mårtensson, L.-E. Eriksson, and P. Albråten. “Numerical simulations of unsteady wakeflow”. *The 10th ISABE meeting, Nottingham, United Kingdom*. 1991.
- [41] F. Menter. Stress-blended eddy simulation (SBES) - A new paradigm in hybrid RANS-LES modeling. *Notes on Numerical Fluid Mechanics and Multidisciplinary Design* (2018), 27–37.
- [42] F. R. Menter. Two-equation eddy-viscosity turbulence models for engineering applications. *AIAA journal* **32**.8 (1994), 1598–1605.
- [43] F. Menter. *Best Practice: Scale-Resolving Simulations in ANSYS CFD*. Tech. rep. 2. ANSYS Germany GmbH, 2015.
- [44] E. M. J. Naylor et al. Optimization of Nonaxisymmetric Endwalls in Compressor S-Shaped Ducts. *ASME. Journal of Turbomachinery* **133**.1 (2011), 011012. DOI: 10.1115/1.3103927.
- [45] E. M. Naylor et al. Optimization of nonaxisymmetric endwalls in compressor S-shaped ducts. *Journal of Turbomachinery* **132**.1 (2010), 1–10. ISSN: 0889504X. DOI: 10.1115/1.3103927.
- [46] F. Nicoud F. Ducros. Subgrid-Scale Stress Modelling Based on the Square of the Velocity Gradient Tensor. *Flow, Turbulence and Combustion* **62** (1999), 183–200.
- [47] C. Ortiz Duen˜as et al. “Effect of Length on Compressor Inter-Stage Duct Performance”. *Volume 6: Turbo Expo 2007, Parts A and B*. ASMEDC, 2007, pp. 319–329. ISBN: 0-7918-4795-0. DOI: 10.1115/GT2007-27752. URL: <https://asmedigitalcollection.asme.org/GT/proceedings/GT2007/47950/319/363713>.
- [48] A. Probst et al. “A Comparison of Detached-eddy Simulation and Reynolds-stress Modelling Applied to the Flow over a Backward-facing Step and an Airfoil at Stall”. *48th AIAA Aerospace Sciences Meeting Including the New Horizons Forum and*

- Aerospace Exposition, Aerospace Sciences Meetings*. AIAA 2010-920. AIAA. 2010, pp. 1–18. DOI: doi:10.2514/6.2010-920.
- [49] O. P. Sharma and T. L. Butler. Predictions of endwall losses and secondary flows in axial flow turbine cascades. *Journal of Turbomachinery* **109.2** (1987), 229–236. ISSN: 15288900. DOI: 10.1115/1.3262089.
- [50] M. Shur et al. Detached-eddy simulation of an airfoil at high angle of attack. *Engineering Turbulence Modelling and Experiments 4* **4** (1999), 669–678. DOI: 10.1016/B978-008043328-8/50064-3.
- [51] E. M. V. Siggeirsson and N. Andersson. “The NASA 2D wall-mounted hump simulated using DDES-SA with the G3D::Flow solver”. *AIAA Scitech 2019 Forum*. San Diego, California, 2019.
- [52] E. M. V. Siggeirsson, N. Andersson, and M. O. Burak. “Integrated Compressor Duct with Bleed: Experimental Validation of a Hybrid RANS/LES Approach”. *24th ISABE Conference*. Canberra, Australia, 2019.
- [53] E. M. V. Siggeirsson, N. Andersson, and M. O. Burak. Numerical and Experimental Aerodynamic Investigation of an S-shaped Intermediate Compressor Duct with Bleed. *Accepted for publication in Journal of Turbomachinery* (2020).
- [54] E. M. V. Siggeirsson, N. Andersson, and M. O. Burak. “Off design simulations of an S-shaped intermediate compressor duct: Experimental validation of DDES and RANS using G3D::Flow”. *AIAA Scitech 2020 Forum*. 2020.
- [55] E. M. V. Siggeirsson, N. Andersson, and M. Lejon. Integrated compressor duct aerodynamics with an integrated rotor off-take bleed. *Submitted to an AIAA Journal* ().
- [56] E. M. V. Siggeirsson, N. Andersson, and F. Wallin. “Numerical and experimental study on bleed impact on intermediate compressor duct performance”. *ASME 2018, Turbo Expo*. Oslo, Norway, 2018.
- [57] E. M. V. Siggeirsson, N. Andersson, and F. Wallin. “Sensitivity study of the SA-DDES shielding function”. *AIAA Scitech 2018 Forum*. Kissimmee, Florida, 2018.
- [58] E. M. V. Siggeirsson. *Integrated Duct Aerodynamics*. Licentiate Thesis, Chalmers University of Technology. 2018.
- [59] J. SMAGORINSKY. General circulation experiments with the primitive equations: I. The basic experiment. *Monthly weather review* **91.3** (1963), 99–165. DOI: 10.1175/1520-0493(1963)091<0099:GCEWTP>2.3.CO;2.
- [60] T. Sonoda, T. Arima, and M. Oana. The effect of inlet boundary layer thickness on the flow within an annular S-shaped duct. *Proceedings of the ASME Turbo Expo* **1**. July (1998). DOI: 10.1115/98-GT-260.
- [61] P. R. Spalart. *Young-Person’s Guide to Detached-Eddy Simulation Grid*. Tech. rep. NASA/CR-2001-211032. Moffett Field, CA, USA: NASA Langley Technical Report Server, 2001.
- [62] P. R. Spalart and S. R. Allmaras. “A one-equation turbulence model for aerodynamic flows”. *30th Aerospace Sciences Meeting and Exhibit, Aerospace Sciences Meetings*. Vol. 1. 1992, pp. 5–21. DOI: 10.2514/6.1992-439.
- [63] P. R. Spalart, F. T. Johnson, and S. R. Allmaras. “Modifications and Clarifications for the Implementation of the Spalart-Allmaras Turbulence Model”. *Seventh Inter-*

- national Conference on Computational Fluid Dynamics (ICCFD7)*. ICCFD7-1902. Haway, 2012, pp. 1–11.
- [64] P. R. Spalart et al. A new version of detached-eddy simulation, resistant to ambiguous grid densities. *Theoretical Computational Fluid Dynamics* **20** (2006), 181–195. DOI: 10.1007/s00162-006-0015-0.
- [65] P. R. Spalart et al. “Comments on the Feasibility of LES for Wings, and on a Hybrid RANS/LES Approach”. *Proceedings of first AFOR International Conference on DNS/LES*. edited by C. Liu and Z. Liu. Ruston, Louisiana: Greyden Press, 1997, pp. 137–147.
- [66] T Stürzebecher et al. “Automated Aerodynamic Optimization of an Aggressive S-Shaped Intermediate Compressor Duct”. *Volume 2D: Turbomachinery*. American Society of Mechanical Engineers, 2018, pp. 1–11. ISBN: 978-0-7918-5102-9. DOI: 10.1115/GT2018-75184. URL: <https://asmedigitalcollection.asme.org/GT/proceedings/GT2018/51029/Oslo,Norway/272455>.
- [67] R. Swanson and E. Turkel. Multistage Schemes With Multigrid for Euler and Navier-Stokes Equations (Dec. 1997).
- [68] R. Swanson, E. Turkel, and C.-C Rossow. Convergence acceleration of Runge–Kutta schemes for solving the Navier–Stokes equations. *Journal of Computational Physics* **224** (May 2007), 365–388. DOI: 10.1016/j.jcp.2007.02.028.
- [69] J. V. Taylor. Separated Flow Topology in Compressors. *Journal of Turbomachinery* **141.9** (2019), 1–9. ISSN: 0889-504X. DOI: 10.1115/1.4044132.
- [70] J. V. Taylor and R. J. Miller. Competing three-dimensional mechanisms in compressor flows. *Journal of Turbomachinery* **139.2** (2017), 1–10. ISSN: 15288900. DOI: 10.1115/1.4034685.
- [71] E. Turkel and V. Vatsa. Choice of Variables and Preconditioning for Time Dependent Problems (June 2003). DOI: 10.2514/6.2003-3692.
- [72] E. Turkel and V. Vatsa. Local preconditioners for steady and unsteady flow applications. <http://dx.doi.org/10.1051/m2an:2005021> **39** (May 2005). DOI: 10.1051/m2an:2005021.
- [73] V. N. Vatsa, D. P. Lockard, and P. R. Spalart. Grid Sensitivity of SA-Based Delayed-Detached-Eddy-Simulation Model for Blunt-Body Flows. *AIAA Journal* **55.8** (2017), 2842–2847. DOI: 10.2514/1.J055685.
- [74] A. D Walker, A. G Barker, and J. F Carrotte. “Numerical design and experimental evaluation of an aggressive s-shaped compressor transition duct with bleed”. *ASME 2011 Turbo Expo: Turbine Technical Conference and Exposition*. Vol. 7: Turbomachinery, Part A. American Society of Mechanical Engineers. 2011, pp. 151–161. DOI: 10.1115/GT2011-45628.
- [75] A. D. Walker et al. “An aggressive S-shaped compressor transition duct with swirling flow and aerodynamic lifting struts”. *ASME Turbo Expo 2014: Turbine Technical Conference and Exposition*. American Society of Mechanical Engineers Digital Collection. 2014.
- [76] A. D. Walker et al. Integrated outlet guide vane design for an aggressive S-shaped compressor transition duct. *Journal of Turbomachinery* **135.1** (2013), 011035.